

A mechanically driven form of Kirigami as a route to 3D mesostructures in micro/nanomembranes

Yihui Zhang^{a,1}, Zheng Yan^{b,1}, Kewang Nan^c, Dongqing Xiao^d, Yuhao Liu^b, Haiwen Luan^e, Haoran Fu^{e,f}, Xizhu Wang^b, Qinglin Yang^b, Jiechen Wang^b, Wen Ren^g, Hongzhi Si^b, Fei Liu^a, Lihen Yang^b, Hejun Li^g, Juntong Wang^c, Xuelin Guo^b, Hongying Luo^{e,h}, Liang Wang^{e,i}, Yonggang Huang^{e,2}, and John A. Rogers^{b,d,j,2}

^aCenter for Mechanics and Materials, Applied Mechanics Laboratory (AML), Department of Engineering Mechanics, Tsinghua University, Beijing 100084, People's Republic of China; ^bDepartment of Materials Science and Engineering and Frederick Seitz Materials Research Laboratory, University of Illinois at Urbana-Champaign, Urbana, IL 61801; ^cDepartment of Mechanical Science and Engineering, University of Illinois at Urbana-Champaign, Urbana, IL 61801; ^dDepartment of Chemistry, University of Illinois at Urbana-Champaign, Urbana, IL 61801; ^eDepartments of Civil and Environmental Engineering and Mechanical Engineering, Center for Engineering and Health, and Skin Disease Research Center, Northwestern University, Evanston, IL 60208; ^fDepartment of Civil Engineering and Architecture, Zhejiang University, Hangzhou 310058, People's Republic of China; ^gDepartment of Chemical and Biomolecular Engineering, University of Illinois at Urbana-Champaign, Urbana, IL 61801; ^hInstitute of Applied Mechanics, School of Aerospace Engineering and Applied Mechanics, Tongji University, Shanghai 200092, People's Republic of China; ⁱInstitute of Chemical Machinery and Process Equipment, Department of Chemical and Biological Engineering, Zhejiang University, Hangzhou 310027, People's Republic of China; and ^jDepartment of Materials Science and Engineering, Beckman Institute for Advanced Science and Technology, University of Illinois at Urbana-Champaign, Urbana, IL 61801

This contribution is part of the special series of Inaugural Articles by members of the National Academy of Sciences elected in 2015.

Contributed by John A. Rogers, August 7, 2015 (sent for review July 14, 2015; reviewed by Michael David Dickey and Shu Yang)

Assembly of 3D micro/nanostructures in advanced functional materials has important implications across broad areas of technology. Existing approaches are compatible, however, only with narrow classes of materials and/or 3D geometries. This paper introduces ideas for a form of Kirigami that allows precise, mechanically driven assembly of 3D mesostructures of diverse materials from 2D micro/nanomembranes with strategically designed geometries and patterns of cuts. Theoretical and experimental studies demonstrate applicability of the methods across length scales from macro to nano, in materials ranging from monocrystalline silicon to plastic, with levels of topographical complexity that significantly exceed those that can be achieved using other approaches. A broad set of examples includes 3D silicon mesostructures and hybrid nanomembrane-nanoribbon systems, including heterogeneous combinations with polymers and metals, with critical dimensions that range from 100 nm to 30 mm. A 3D mechanically tunable optical transmission window provides an application example of this Kirigami process, enabled by theoretically guided design.

Kirigami | three-dimensional assembly | buckling | membranes

Three-dimensional micro/nanostructures are of growing interest (1–10), motivated by their increasingly widespread applications in biomedical devices (11–13), energy storage systems (14–19), photonics and optoelectronics (20–24), microelectromechanical systems (MEMS) (25–27), metamaterials (21, 28–32), and electronics (33–35). Of the many methods for fabricating such structures, few are compatible with the highest-performance classes of electronic materials, such as monocrystalline inorganic semiconductors, and only a subset of these can operate at high speeds, across length scales, from centimeters to nanometers. For example, although approaches (36–39) that rely on self-actuating materials for programmable shape changes provide access to a wide range of 3D geometries, they apply only to certain types of materials [e.g., gels (36, 37), liquid crystal elastomers (39), and shape memory alloys (38)], generally not directly relevant to high-quality electronics, optoelectronics, or photonics. Techniques that exploit bending/folding of thin plates via the action of residual stresses or capillary effects are, by contrast, naturally compatible with these modern planar technologies, but they are currently most well developed only for certain classes of hollow polyhedral or cylindrical geometries (1, 10, 40–44). Other approaches (45, 46) rely on compressive buckling in narrow ribbons (i.e., structures with lateral aspect ratios of >5:1) or filaments to yield complex 3D structures, but of primary utility in open-network mesh type layouts. Attempts to apply this type of scheme

to sheets/membranes (i.e., structures with lateral aspect ratios of <5:1) lead to “kink-induced” stress concentrations that cause mechanical fracture. The concepts of Kirigami, an ancient aesthetic pursuit, involve strategically configured arrays of cuts to guide buckling/folding processes in a manner that reduces such stresses, to enable broad and interesting classes of 3D structures, primarily in paper at centimeter and millimeter dimensions. Traditional means for defining these cuts and for performing the folds do not extend into the micro/nanoscale regime, nor do they work effectively with advanced materials, particularly brittle semiconductors. This paper introduces ideas for a form of Kirigami that can be used in these contexts. Here, precisely controlled compressive forces transform 2D micro/nanomembranes with lithographically defined geometries and patterns of cuts into 3D structures across length scales from macro to micro and nano, with levels of complexity and control that significantly exceed those that can be achieved with alternative methods. This Kirigami approach is

Significance

Existing options in three-dimensional (3D) assembly of micro/nanomaterials are constrained by a narrow accessible range of materials and/or 3D geometries. Here we introduce concepts for a form of Kirigami for the precise, mechanically driven assembly of 3D mesostructures from 2D micro/nanomembranes with strategically designed geometries and patterns of cuts. Theoretical and experimental studies in a broad set of examples demonstrate the applicability across length scales from macro to micro and nano, in materials ranging from monocrystalline silicon to metal and plastic, with levels of topographical complexity that significantly exceed those possible with other schemes. The resulting engineering options in functional 3D mesostructures have important implications for construction of advanced micro/nanosystems technologies.

Author contributions: Y.Z., Z.Y., Y.H., and J.A.R. designed research; Y.Z., Z.Y., K.N., D.X., Y.L., H. Luan, H.F., X.W., Q.Y., Jiechen Wang, W.R., H.S., F.L., L.Y., H. Li, Juntong Wang, X.G., H. Luo, and L.W. performed research; Y.Z., Z.Y., Y.H., and J.A.R. analyzed data; and Y.Z., Z.Y., Y.H., and J.A.R. wrote the paper.

Reviewers: M.D.D., North Carolina State University; and S.Y., University of Pennsylvania.

The authors declare no conflict of interest.

¹Y.Z. and Z.Y. contributed equally to this work.

²To whom correspondence may be addressed. Email: jrogers@illinois.edu or y-huang@northwestern.edu.

This article contains supporting information online at www.pnas.org/lookup/suppl/doi:10.1073/pnas.1515602112/-DCSupplemental.

by narrow joints. Here, the outer squares attach to small rectangular anchors that adhere strongly to a biaxially prestrained elastomer substrate through covalent surface chemical bonding. All other regions release from the substrate via elimination of a sacrificial interface layer, as described in *Methods*. Relaxing the prestrain generates compressive stresses that induce these regions to buckle out of the plane, as shown in an intermediate state of assembly [results from finite-element analysis (FEA); Fig. 1A, *Center Left*]. The final configuration corresponds to that of a square cuboid, as given by the FEA result in Fig. 1A, *Center Right* and the scanning electron micrograph (SEM) (colorized; Fig. 1A, *Right*). The color indicates the maximum principal strains. Peak values remain well below the fracture thresholds ($\sim 2\%$) for the Si NMs, owing to the stress-reducing effects of the Kirigami cuts that form the narrow hinges between the sides. (The silicon is assumed to exhibit linear responses up to strains that approach the fracture point.) A failure criterion based on the maximum principal strain is adopted here for simplicity, in which the threshold is assumed to be independent of thickness, for membrane thicknesses down to ~ 100 nm. The dimensions of the anchor regions must be carefully selected to avoid delamination and surface buckling. In choosing patterns of cuts, the locations should (i) eliminate localized deformations that might occur otherwise and (ii) avoid any possible self-locking of different subcomponents during the compressive buckling. The cuts also play critical roles in defining the final 3D geometries. Fig. 1B shows an example in which a cross-cut pattern divides a large square into four smaller ones. Here, assembly forms a curved pyramidal mesostructure. Repeated implementation of

such crosses (Fig. 1B) in the subsquares (i.e., the smaller squares) yields a fractal-inspired pattern of cuts (51) that divides the original square into interconnected small pieces with similar shapes and sizes. The resulting 3D structure adopts a highly complex configuration, where bending and twisting deformations localize at the joints defined by the cuts, with strains that remain below the fracture threshold. The image in Fig. 1C, *Right* and those in *SI Appendix*, Fig. S3 offer multiple viewing angles. Many other geometries are possible, including those with circular symmetry, as shown in Fig. 1D and E. The latter case has a well-defined chirality, set by the configuration of Kirigami cuts. In all cases examined in this paper, 2D precursors without carefully placed cuts tend to undergo sharp, localized deformations with associated stress concentrations (*SI Appendix*, Fig. S4) that lead to fracture. For unpatterned, circular 2D precursors, the maximum strains reach values that are nearly 4 times larger than those with Kirigami designs under otherwise similar conditions. Consequently, even at the largest level of prestrain ($\sim 35\%$) that can be accommodated without cuts, the corresponding maximum 3D extension is small (*SI Appendix*, Fig. S5A), as defined by the aspect ratio, $\alpha = d_{\text{out-of-plane}}/d_{\text{in-plane}}$, where $d_{\text{out-of-plane}}$ and $d_{\text{in-plane}}$ denote the maximum out-of-plane dimension and in-plane extent, respectively. Specifically, the value of α without Kirigami cuts (0.3) is nearly 2.5 times smaller than that achievable with cut geometries demonstrated in Fig. 1D and E and *SI Appendix*, Fig. S5B.

These concepts can be implemented across a broad range of lengths scales, with nearly any type of material, and in systems that include filamentary 3D networks and/or hierarchical layouts.

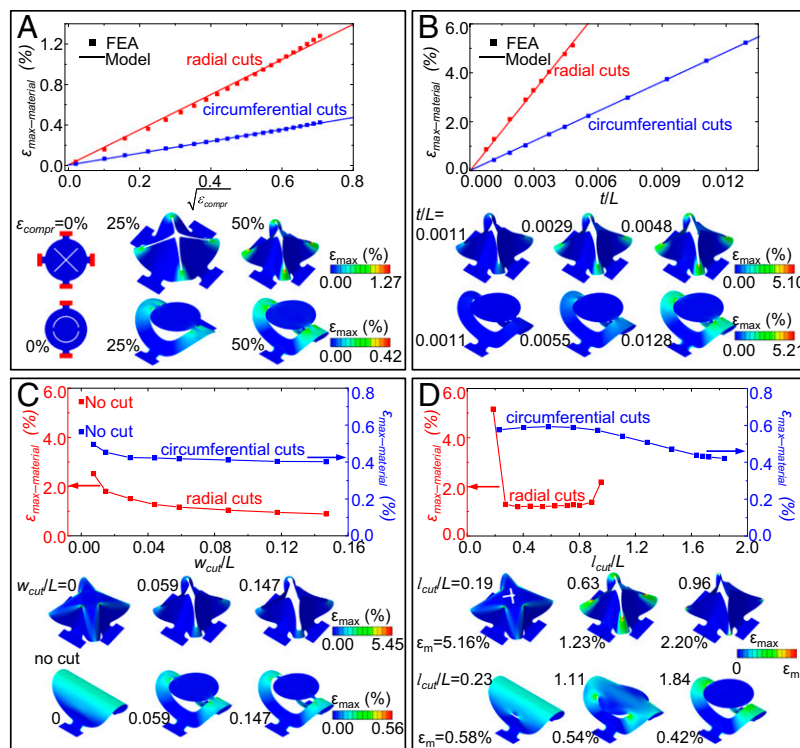


Fig. 2. Computational results that highlight fundamental aspects of Kirigami designs in examples with purely radial and purely circumferential cuts. (A) Maximum material strain as a function of the square root of the compressive strain for membranes with $t/L = 0.0011$, $w_{\text{cut}}/L = 0.044$, and $l_{\text{cut}}/L = 1.68$ (for circumferential cuts) or 0.76 (for radial cuts) and the associated strain distributions. (B) Maximum material strain as a function of the dimensionless thickness for membranes with $w_{\text{cut}}/L = 0.044$ and $l_{\text{cut}}/L = 1.68$ (for circumferential cuts) or 0.76 (for radial cuts), under a compressive strain of 50%, and the associated strain distributions. (C) Maximum material strain as a function of the dimensionless widths of Kirigami cuts in membranes with $t/L = 0.0011$ and $l_{\text{cut}}/L = 1.68$ (for circumferential cuts) or 0.76 (for radial cuts), under a compressive strain of 50%, and the associated strain distributions. (D) Maximum material strain as a function of the dimensionless cut lengths for membranes with $t/L = 0.0011$ and $w_{\text{cut}}/L = 0.044$, under a compressive strain of 50%, and the associated strain distributions. In all cases, the color in the FEA results corresponds to the magnitude of the maximum principal strain.

An example of a polymer structure appears in Fig. 1*F*, where a Kirigami-based circular pattern connects to serpentine ribbons organized in a circular, closed form to yield an elaborate 3D mesostructure that resembles a jellyfish (Fig. 1*F*). The buckling begins with the ribbons at the periphery, followed by the eight straight ribbons in the central circular membrane, leading to a 3D configuration with multiple levels. Fig. 1*G* shows structures that have characteristic dimensions ranging from 100 nm (thickness of the bare Si NM in the example in Fig. 1*G*, *Left*) to ~ 30 mm (lateral dimensions of the 3D plastic sheet in Fig. 1*G*, *Right*), each overlaid with results from FEA simulations. Throughout all examined geometries, materials, and length scales, experimental results exhibit excellent quantitative agreement with FEA predictions, thereby establishing computation as a means for rapid design iterations, as demonstrated subsequently in the engineering of a tunable optical device. The 2D precursors of all examples in Fig. 1 are in *SI Appendix*, Fig. S6.

FEA can also reveal the dependence of the maximum principal strains on the prestrain in the elastomer substrate, as a function of geometric parameters related to the membrane structure and Kirigami cuts, as shown in Fig. 2. During lateral buckling, the 2D precursors undergo complex out-of-plane bending deformations, with associated spatially dependent variations in the curvature. The maximum strains occur at locations with highest change in curvature; these locations typically remain constant throughout the buckling process. Quantitative analyses of representative Kirigami patterns (Fig. 2*A* and *B*) with purely radial and circumferential cuts show that the maximum strains ($\epsilon_{\text{max-material}}$) are proportional to the normalized thickness for a single-layer Si membrane, i.e., t/L , where L measures the overall dimension of the 2D precursor (e.g., the radii of the circular geometries in Fig. 2), and the square root of the compressive strain (ϵ_{compr}) applied to the 2D precursor, where $\epsilon_{\text{compr}} = \epsilon_{\text{pre}}/(1 + \epsilon_{\text{pre}})$. This scaling, i.e., $\epsilon_{\text{max-material}} \propto t\sqrt{\epsilon_{\text{compr}}}/L$, also applies to the other 3D structures examined here (*SI Appendix*, Figs. S7 and S8), including those with various Kirigami cuts (e.g.,

antisymmetric cuts in a serpentine configuration or with combinations of radial and circumferential cuts) as well as uniaxial and biaxial prestrains in the elastomer substrate. Although the effect of the widths of the cuts (w_{cut}) cannot be captured with a simple scaling law, the qualitative dependence consistently involves a decrease in the maximum strain with an increase in w_{cut} (e.g., Fig. 2*C* and *SI Appendix*, Fig. S9). This trend further highlights the critical, enabling role of Kirigami concepts in this approach to 3D assembly. The effect of cut length is even more complicated, partly because this parameter significantly affects the nature of deformation modes in a qualitative sense, as shown in the results of Fig. 2*D* and *SI Appendix*, Fig. S10. These calculations indicate, in fact, that the lengths must be sufficiently large to avoid stress concentrations (e.g., in Fig. 2*D* and *SI Appendix*, Fig. S10*B* and *D*). These qualitative and quantitative rules, together with the high accuracy in the FEA, provide a strong foundation for systematic, engineering design.

Three-Dimensional Mesostructures in Membranes and in Membranes/Ribbons, with Diverse Geometries.

Fig. 3 presents a collection of experimental results and FEA predictions for dozens of 3D structures formed with Si NM/polymer precursors (both layers, 300 nm in thickness). The nature of the Kirigami cuts in the 2D precursors provides the basis for a classification scheme: (i) membranes without any cuts, (ii) membranes with symmetric cuts, (iii) membranes with antisymmetric cuts, and (iv) membranes with asymmetric cuts. Without cuts (Fig. 3*A*), the bonding locations, the overall shapes, and/or the addition of holes must be selected carefully to avoid the type of stress concentrations mentioned previously. These considerations impose tight restrictions on the 3D geometries that are possible. Kirigami cuts avoid these constraints, such that even for a given overall membrane shape and set of bonding locations, as shown in Fig. 3*B–D* (except for the last two designs in Fig. 3*B*), a rich range of 3D topologies can be realized. For circular shapes, cuts along the radial or circumferential directions serve as the basis for

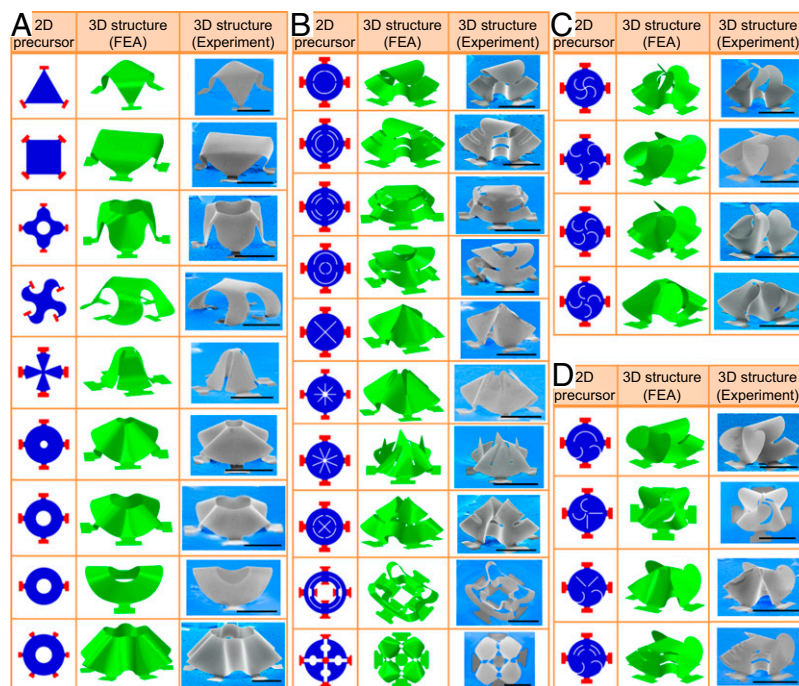


Fig. 3. Experimental and computational studies of various 3D silicon/polymer mesostructures and their classification according to geometric characteristics of the Kirigami cuts. (A–D) Two-dimensional precursors, SEM images, and FEA predictions for 27 3D mesostructures formed with precursor patterns without any cuts (A), with symmetric cuts (B), with antisymmetric cuts (C), and with asymmetric cuts (D). (Scale bars, 200 μm .)

symmetric Kirigami patterns. Cuts with serpentine configurations provide antisymmetric examples. Fig. 3 *B–D* demonstrates how the orientations of the cuts dictate the assembly process. Including additional bonding locations at the inner regions of the precursors further enhances the spatial variations in the modes of deformation. The last two cases in Fig. 3*B* provide examples where the positions of holes help to avoid self-contact of the membrane during the 3D assembly.

As demonstrated in Fig. 1, these Kirigami concepts can naturally include ribbon-shaped precursors (46), to yield complex 3D structures, including those with multiple levels of buckling. Fig. 4*A* and *SI Appendix, Fig. S11* present an additional 12 examples. For the first 5 (i.e., 4 in Fig. 4*A, Left* and 1 in Fig. 4*A, Top Right*), buckling occurs first in the membranes; these motions then induce compression in the supported ribbons, leading to subsequent buckling processes. The first structure represents an exception, where the untethered ends of the ribbons allow freedom of motion, with little intrinsic deformation throughout the assembly process. Here, the ribbons simply follow the supporting membranes, to final orientations that are almost perpendicular to the plane of substrate. In such designs, the ribbons

have negligible effects on the 3D configurations of the membranes. The three examples in Fig. 4*A, Upper Middle, Lower Middle, and Bottom Right* represent cases where buckled ribbons play an essential role in the assembly, via their selective bonding to the substrate, to form a first level of construction. Membranes raised upward by these ribbons form a second level. The comparatively high stiffnesses of the membranes affect deformations of the supporting ribbons, as evidenced by their rotation with respect to the corresponding length directions.

Using the membrane and/or hybrid membrane–ribbon configurations as building blocks, arrays or nested architectures can be formed, as shown in Fig. 4*B*. Fig. 4*B, Top Left* involves an evenly spaced, triangular collection of double-level membrane–ribbon mesostructures (in Fig. 4*A*), with five unit cells along each edge. Fig. 4*B, Top Center* shows a double-level architecture that resembles a “crown,” achieved with a 2D precursor illustrated in *SI Appendix, Fig. S12A*. Images at multiple view angles (*SI Appendix, Fig. S12B*) highlight the geometrical complexity. The third example (Fig. 4*B, Top Right*) represents a triangular array of membrane–ribbon mesostructures with raised circular disks that adopt nearly planar shapes, owing to their relatively large stiffnesses. Fig. 4*B, Bottom* corresponds to a mixed array composed of six membrane mesostructures without any cuts (in two different configurations), another four membrane mesostructures with antisymmetric cuts (with opposite chirality), and six hybrid membrane–ribbon mesostructures (in two different configurations). All of these results agree well with FEA predictions.

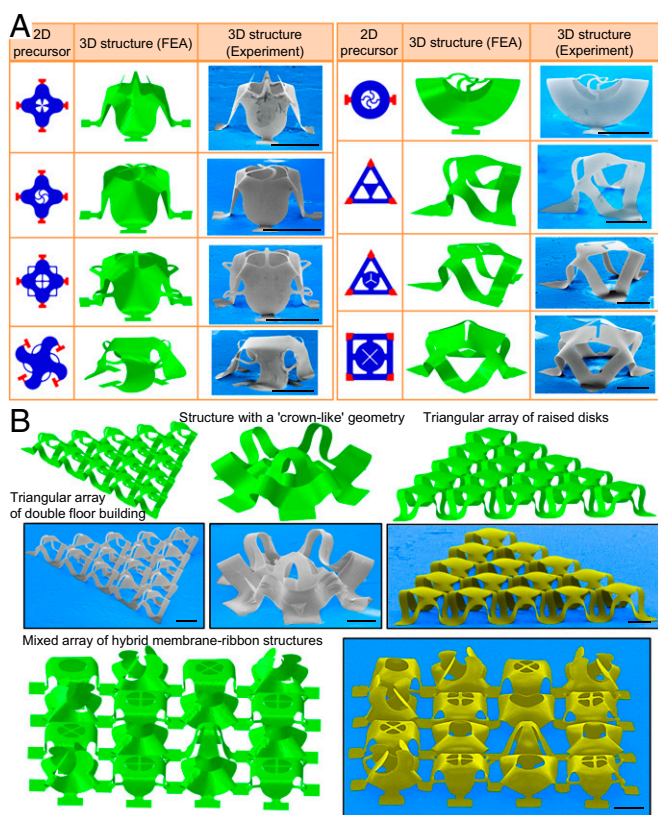


Fig. 4. Experimental and computational studies of 3D mesostructures with hybrid membrane–ribbon configurations and extended array architectures. (A) Two-dimensional precursors, FEA predictions, and SEM images for five 3D membrane–ribbon hybrid mesostructures (four on *Left* and one on *Top Right*) that are supported by 3D membranes and three 3D membrane–ribbon hybrid mesostructures (*Upper Middle, Lower Middle, and Bottom Right*) that are supported by ribbons. All of these structures incorporate bilayers of silicon/polymer (each ~300 nm in thickness). (B) Array architectures that include interconnected collections of 3D mesostructures with identical or similar configurations to those in Fig. 3 and in A. The first two of these use silicon/polymer bilayers (each ~300 nm in thickness for the first structure; ~300 nm in silicon thickness and 2 μm in SU8 thickness for the second structure), and the others use polymer membranes (~4 μm in thickness). (Scale bars, 200 μm.)

Three-Dimensional Mesostructures in Different Materials and Geometries and with Supported Micro/Nanopatterns.

The physical nature of the Kirigami assembly process allows immediate application across a broad range of material types. Fig. 5 *A* and *B* presents examples, including those formed using both polymers and metals (Au), with membrane or hybrid membrane–ribbon configurations. Corresponding 2D precursors appear in *SI Appendix, Fig. S13*. Additional examples are in *SI Appendix, Figs. S14* and *S15*. All of the structures in Fig. 3 reproduced in millimeter-scale plastic models are shown in *SI Appendix, Fig. S16*. Heterogeneous combinations of different materials are also possible, with two examples constructed with polymers and silicon in Fig. 5*C*. Furthermore, buckled membranes can be exploited as 3D platforms (with curved surfaces), for micro/nanopatterns of other materials, as demonstrated in polymer–silicon (Fig. 5*D*) and polymer–metal (Fig. 5*E*). In particular, Fig. 5*D* shows a square array of silicon nanodisks (~200 nm in thickness, ~200 nm in diameter) formed by soft lithography (*SI Appendix, Fig. S17*) on a 2D polymer precursor that transforms into a 3D structure with three untethered ribbons. Fig. 5*E, Left* corresponds to a square array of Au microdisks (~50 nm in thickness, ~5 μm in diameter) distributed across the area of a 2D precursor. The array follows the curved surfaces of the 3D architecture that forms by Kirigami assembly. Fig. 5*E, Center Left* involves a spiral pattern of Au microdisks (~50 nm in thickness, ~10 μm in diameter), consisting of eight unevenly spaced branches (each with ~20 microdisks) that adapt to the antisymmetric cuts of the supporting polymer membrane. The assembly process projects these patterns onto four petal-shaped structures, thereby placing them in a 3D configuration. Fig. 5*E, Center Right* is an example with the configuration of a square space-filling tree (with fifth order) as a complex Au network (with 5 μm width for each wire) that is then transformed into a 3D spatial form. Fig. 5*E, Right* corresponds to third-order fractal Cayley tree (52) microstructures (Au, ~5 μm width for each wire) on a 3D membrane with four identical parts. Similar hybrid architectures with first- and second-order Cayley tree configurations are in *SI Appendix, Fig. S18 A* and *B*. Two additional examples with an array of Au microdisks assembled in a 3D polymer layout appear in *SI Appendix, Fig. S18 C* and *D*.

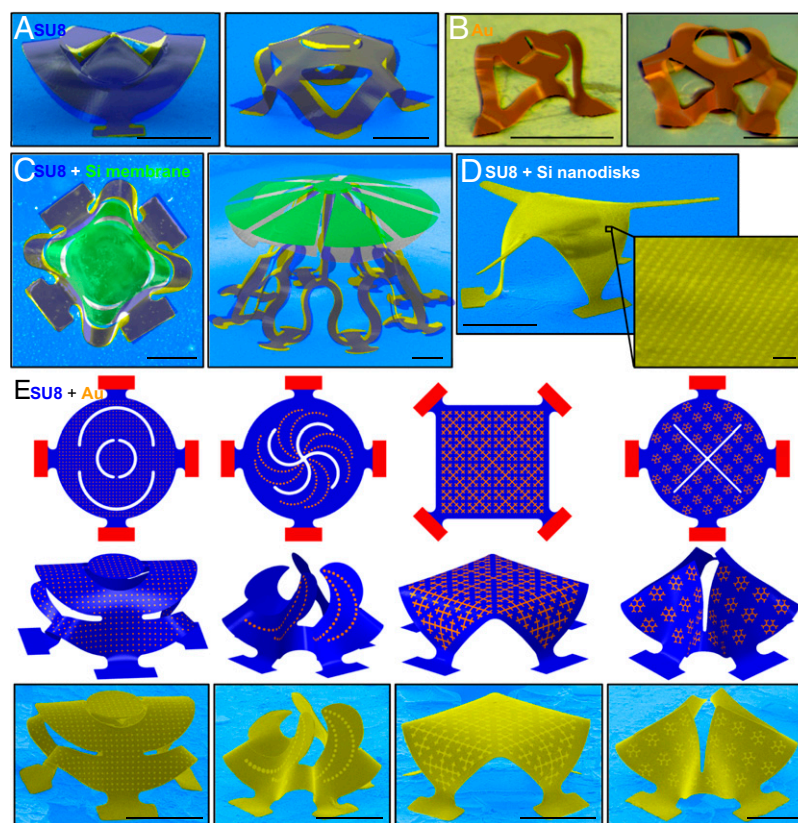


Fig. 5. Three-dimensional mesostructures of membrane and hybrid membrane-ribbon configurations with various material compositions. (A and B) Experimental images and overlaid FEA predictions of 3D mesostructures made of polymer and metal (Au). (Scale bars, 200 μm .) (C) Three-dimensional membrane mesostructures with heterogeneous combinations of silicon and polymer. (Scale bars, 200 μm .) (D) Three-dimensional membrane mesostructures consisting of a polymer membrane with a patterned array of silicon nanodisks on the surface, with a magnified view in *Inset*. (Scale bar, 200 μm ; in *Inset*, 1 μm .) (E) Related 3D mesostructures with patterned arrays of Au microstructures. (Scale bars, 200 μm .)

A Mechanically Tunable Optical Transmission Window. The ability to dynamically and reversibly change the 3D shapes represents an important functional option associated with all of the mesostructures described previously. Fig. 6 provides a device demonstration in the form of a mechanically tunable optical transmission window (with a 3×3 array of shutter-like structures). A representative element (Fig. 6A, *Top*) consists of a reflective membrane ($\sim 50\text{-nm}$ -thick Au on an $\sim 8\text{-}\mu\text{m}$ -thick layer of SU8) in a square shape, with two nonpenetrating Kirigami cuts. The two ends bond to a transparent, uniaxially prestrained elastomer substrate at rectangular anchors. Compressive buckling of the central ribbon forces rotational motion of the membrane, as shown by both experiment and FEA results in an intermediate state of assembly (Fig. 6A, *Middle*). As the membranes rotate upward, they block a decreasing fraction of normally incident light. FEA simulations identify a level of prestrain ($\sim 90\%$) that maximizes the range over which the transmittance can be tuned in this fashion. Here, the membranes, in their fully rotated state, are nearly perpendicular to the plane of the elastomer substrate (Fig. 6A, *Bottom*). The optical micrographs and FEA images show excellent agreement for both the intermediate and final states of assembly. Fig. 6B presents a variation of this design, in which short segments ($\sim 17\%$) in the centers of the ribbons have increased thicknesses (corresponding to a double layer of $\sim 50\text{-nm}$ -thick Au and $\sim 23\text{-}\mu\text{m}$ -thick SU8). This structure offers greatly enhanced rotations for a given level of strain, as a consequence of the reduced curvature in the thickened regions of the ribbons. Here, the thin segments accommodate an increased level of deformation. Experiment and FEA results (Fig. 6B, *Middle* and *Bottom*) illustrate this characteristic. Consequently, a

comparatively low level of prestrain ($\sim 66\%$) actuates the full, 90° rotation of the membrane.

Fig. 6C shows measurements and modeling results for the dependence of optical transmittance on the uniaxial tensile strain (ϵ_{appl}) applied to the elastomeric substrate for these two different designs. The illumination spot (diameter $\sim 1.0\text{ mm}$) covers the entire active area throughout the experiments. In both cases, the optical transmittance decreases monotonically from $\sim 97\%$ in the zero-strain state to $\sim 22\%$ at the critical state ($\epsilon_{\text{appl}} = 90\%$ and 66% for the two designs). Linear fits of the data yield metrics (i.e., the slopes of the fitted lines) for the sensitivity of the transmittance to strain, indicating $\sim 40\%$ (relative) increase in sensitivity (~ 1.26 vs. ~ 0.90) enabled by the thickness-modulated design (Fig. 6B). This result indicates the potential of engineering variations in thickness to achieve desired mechanical behaviors. The measured optical properties agree reasonably well with modeling that involves calculation of the optical transmittance associated with 3D geometries predicted by FEA. Three representative states of the nonuniform design appear in Fig. 6C, *Right*. Effects of fatigue do not appear in the optical devices after they are stretched to $\sim 65\%$ strain repetitively at a frequency of $\sim 0.04\text{ Hz}$ for ~ 150 cycles (*SI Appendix*, Fig. S19).

Conclusions

The Kirigami-inspired concepts, design principles, and micro/nanofabrication strategies reported here provide immediate access to diverse 3D membrane architectures with broad-ranging critical dimensions and material compositions, including high-performance semiconductor nanomaterials. The resulting engineering options in functional 3D mesostructures have sweeping implications for

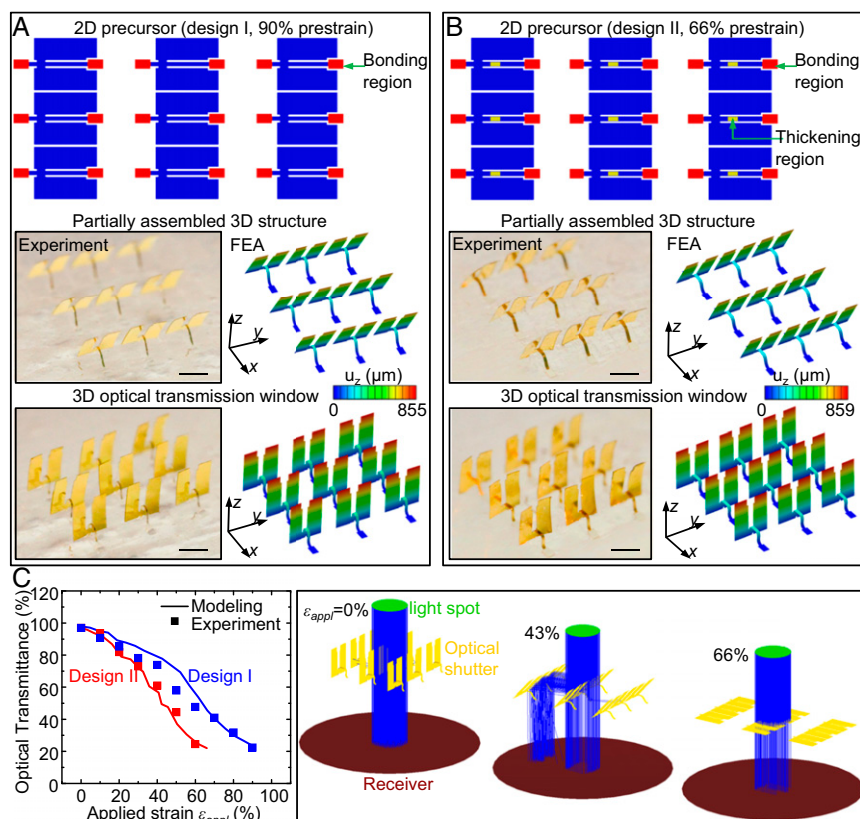


Fig. 6. A mechanically tunable optical transmission window and corresponding measurements and simulations of optical transmittance as a function of applied strain. (A) Schematic illustration of the 2D precursor and its regions of bonding (i.e., red rectangles) (Top), optical micrographs and FEA predictions of the intermediate state (Middle), and final state (Bottom). The color in the FEA results corresponds to the magnitude of the out-of-plane component of the displacement. (B) Similar results for a design with engineered variations in thickness along the length of the support structures. (B, Top) The thick regions appear in yellow. (C) Measured and calculated optical transmittance as a function of uniaxial strain applied to the elastomeric substrate for the devices illustrated in A and B. (C, Right) Illustrations of the simulated light paths for devices with engineered thickness variations, at three different levels of stretching. (Scale bars, 500 μm .)

construction of advanced micro/nanosystems technologies. Additional opportunities may follow from the use of these concepts with fully formed devices, such as waveguides, light sources, and integrated circuits, and/or with 3D structures formed using complementary techniques in 3D printing (16, 53–55).

Methods

Finite-Element Analysis. The calculations used linear buckling analyses of 2D precursor structures under compression to determine the critical buckling strains and corresponding buckling modes. These results served as initial geometric imperfections for postbuckling simulations. Eight-node 3D solid elements and four-node shell elements were used for the substrate and 2D precursor structure, respectively, with refined meshes adopted to ensure the accuracy. The elastic modulus (E) and Poisson’s ratio (ν) are $E_{\text{substrate}} = 166 \text{ kPa}$ and $\nu_{\text{substrate}} = 0.49$ for substrate; $E_{\text{Si}} = 130 \text{ GPa}$ and $\nu_{\text{Si}} = 0.27$ for silicon; $E_{\text{Au}} = 78 \text{ GPa}$ and $\nu_{\text{Au}} = 0.44$ for gold; and $E_{\text{SU8}} = 4.02 \text{ GPa}$ and $\nu_{\text{SU8}} = 0.22$ for SU8.

Fabrication Methods for Silicon, Metals, Polymers, and Combinations of Them.

Preparation of 3D mesostructures of Si NMs/SU8 (both 300 nm in thickness) began with patterning of 2D precursors in the top silicon layer of a silicon-on-insulator (SOI) wafer (300-nm thicknesses of top silicon) by photolithography and reactive ion etching (RIE). After addition of a thin reinforcement layer of a photodefinable epoxy (SU8, 300 nm in thickness) in a geometry to match the patterned silicon, immersion in hydrofluoric acid (HF) removed the buried silicon dioxide (SiO_2) layer from the exposed regions and also slightly from under the edges of the patterns at their periphery. Next, spin casting and photolithography formed patterns of a photoresist (AZ5214, 1.6 μm in thickness) to define the sites for strong bonding in the Kirigami process. Reimmersion in HF completed the removal of the buried oxide by complete

undercut etching. The photoresist at the edge regions tethered the silicon structures to the underlying wafer. Retrieving the structures onto a slab of polydimethylsiloxane (PDMS) (Sylgard 184 silicone elastomer, 1:4) and then transferring them to a water-soluble tape [polyvinyl alcohol (PVA)] oriented the 2D precursors with their top sides facing up, supported by the PVA. Exposing these precursors and a thin silicone elastomer (Dragon Skin, Smooth-On, 0.5 mm in thickness) to UV-induced ozone (UVO) yielded hydroxyl termination on their surfaces. A mechanical stage allowed controlled stretching of the silicone to well-defined levels of prestrain (either uniaxial or biaxial). Laminating the PVA tape with the precursors onto the silicone followed by baking in an oven at 70 $^\circ\text{C}$ for 7 min yielded strong covalent bonds between the silicone and the exposed regions of the silicon. Washing with hot water and then acetone dissolved the PVA tape and the photoresist sacrificial layers. Slowly releasing the prestrain completed the 3D Kirigami assembly process. A schematic illustration of steps is provided in *SI Appendix, Fig. S20*.

Preparation of 3D Si NM (100 nm in thickness) mesostructures involved defining 2D precursors on an SOI wafer (100-nm thicknesses of top silicon) and then following the procedures described above, except without the addition of SU8.

Preparation of 3D mesostructures in polymer membranes started with thermal oxidation to form a layer of SiO_2 (500 nm in thickness) on a silicon wafer. Next, spin casting and photolithography formed 2D precursors of SU8 (4 μm in thickness) on the SiO_2 . Immersion in HF removed the SiO_2 from the exposed regions and also slightly from under the edges of the SU8. Next, spin casting and photolithography formed patterns of photoresist (AZ5214, 1.6 μm in thickness) to define the sites for strong bonding. Reimmersion in HF eliminated the remaining SiO_2 by complete undercut etching. Transfer and bonding steps similar to those used for the Si NM/SU8 structures followed by release of the prestrain completed the assembly process. A schematic illustration of steps is provided in *SI Appendix, Fig. S21*.

Preparation of 3D mesostructures that include both silicon and polymer membranes began with spin casting a layer of photoresist (AZ 5214, 1.6 μm in thickness) on an SOI wafer (300-nm thicknesses of top silicon). Photolithography and RIE etching defined 2D patterns in the top silicon. Next, spin casting and photolithographic patterning formed a thin layer (4 μm in thickness) of SU8, in a distinct geometry spanning both the silicon and other regions. The remaining steps followed the procedures for 3D SU8 mesostructures described above. A schematic illustration is in *SI Appendix, Fig. S22A*.

Preparation of 3D mesostructures of SU8 with arrays of silicon nanodisks began with spin coating of a thin layer (200 nm in thickness) of SU8 on an SOI wafer (200-nm thicknesses of top silicon). Soft imprint lithography using a mold of PDMS with relief in the geometry of cylinders (period 300 nm, diameter 200 nm, height 200 nm) defined corresponding relief in the SU8. RIE etching of the residual layer of SU8 formed isolated disks of SU8 that served as masks for inductively coupled plasma reactive ion etching [Surface Technology Systems (STS)] to define arrays of silicon nanodisks in the top silicon layer. RIE eliminated the remaining SU8. Next, spin casting and photolithography defined patterns of SU8 (4 μm in thickness). The remaining steps followed the procedures for 3D SU8 structures described above. A schematic illustration of steps is in *SI Appendix, Fig. S22B*.

Preparation of 3D mesostructures in metal and polymer hybrid membranes began with thermal oxidation to form a layer of SiO_2 (500 nm in thickness) on

a silicon wafer. Photolithography, electron beam evaporation, and liftoff defined patterns of Cr (5 nm in thickness) and Au (50 nm in thickness) on the SiO_2 . Spin casting formed an adhesion-promoting layer (Omnicoat; Microchemicals, 30 nm in thickness) for spin casting and photolithographic patterning of a thin (4 μm in thickness) layer of SU8 in a geometry matched to the Cr/Au. RIE etching removed the exposed regions of the adhesion-promoting layer. The remaining steps followed the procedures for 3D SU8 structures described above. A schematic illustration of steps is in *SI Appendix, Fig. S23*.

Preparation of mechanically tunable optical transmission windows with uniform thicknesses followed steps similar to those for making 3D structures in hybrid membranes of metal and polymer, except that SU8 with 8- μm thickness was used. Preparation of related structures with thickened regions involved photolithographic patterning of an additional layer of SU8 (15 μm in thickness).

ACKNOWLEDGMENTS. This work was supported by the US Department of Energy, Office of Science, Basic Energy Sciences under Award DE-FG02-07ER46471 and used facilities in the Frederick Seitz Materials Research Laboratory and the Center for Microanalysis of Materials at the University of Illinois at Urbana-Champaign. Y.H. acknowledges support from the National Science Foundation (CMMI-1400169). Y.Z. acknowledges support from the Thousand Young Talents Program of China.

- Shenoy VB, Gracias DH (2012) Self-folding thin-film materials: From nanopolyhedra to graphene origami. *MRS Bull* 37(9):847–854.
- Li F, Josephson DP, Stein A (2011) Colloidal assembly: The road from particles to colloidal molecules and crystals. *Angew Chem Int Ed Engl* 50(2):360–388.
- Damasceno PF, Engel M, Glotzer SC (2012) Predictive self-assembly of polyhedra into complex structures. *Science* 337(6093):453–457.
- Crane NB, Onen O, Carballo J, Ni Q, Guldiken R (2013) Fluidic assembly at the microscale: Progress and prospects. *Microfluid Nanofluidics* 14(3–4):383–419.
- Jang JH, et al. (2007) 3D micro- and nanostructures via interference lithography. *Adv Funct Mater* 17(16):3027–3041.
- Fischer J, Wegener M (2013) Three-dimensional optical laser lithography beyond the diffraction limit. *Laser Photonics Rev* 7(1):22–44.
- Arpin KA, et al. (2010) Multidimensional architectures for functional optical devices. *Adv Mater* 22(10):1084–1101.
- Noorduyn WL, Grinthal A, Mahadevan L, Aizenberg J (2013) Rationally designed complex, hierarchical microarchitectures. *Science* 340(6134):832–837.
- Gao PX, et al. (2005) Conversion of zinc oxide nanobelts into superlattice-structured nanohelices. *Science* 309(5741):1700–1704.
- Huang M, Cavallo F, Liu F, Lagally MG (2011) Nanomechanical architecture of semiconductor nanomembranes. *Nanoscale* 3(1):96–120.
- Tian B, et al. (2012) Macroporous nanowire nanoelectronic scaffolds for synthetic tissues. *Nat Mater* 11(11):986–994.
- Leong TG, et al. (2009) Tetherless thermobiochemically actuated microgrippers. *Proc Natl Acad Sci USA* 106(3):703–708.
- Yu M, et al. (2011) Semiconductor nanomembrane tubes: Three-dimensional confinement for controlled neurite outgrowth. *ACS Nano* 5(4):2447–2457.
- Zhang H, Yu X, Braun PV (2011) Three-dimensional bicontinuous ultrafast-charge and -discharge bulk battery electrodes. *Nat Nanotechnol* 6(5):277–281.
- Pikul JH, Gang Zhang H, Cho J, Braun PV, King WP (2013) High-power lithium ion microbatteries from interdigitated three-dimensional bicontinuous nanoporous electrodes. *Nat Commun* 4:1732.
- Sun K, et al. (2013) 3D printing of interdigitated Li-ion microbattery architectures. *Adv Mater* 25(33):4539–4543.
- Deng J, et al. (2013) Naturally rolled-up C/SiC trilayer nanomembranes as stable anodes for lithium-ion batteries with remarkable cycling performance. *Angew Chem Int Ed Engl* 52(8):2326–2330.
- Pan L, et al. (2012) Hierarchical nanostructured conducting polymer hydrogel with high electrochemical activity. *Proc Natl Acad Sci USA* 109(24):9287–9292.
- Wu H, et al. (2013) Stable Li-ion battery anodes by in-situ polymerization of conducting hydrogel to conformally coat silicon nanoparticles. *Nat Commun* 4:1943.
- Songmuang R, Rastelli A, Mendach S, Schmidt OG (2007) SiO_2/Si radial superlattices and microtube optical ring resonators. *Appl Phys Lett* 90(9):091905.
- Lee JH, et al. (2014) 25th anniversary article: Ordered polymer structures for the engineering of photons and phonons. *Adv Mater* 26(4):532–569.
- Braun PV (2014) Materials chemistry in 3D templates for functional photonics. *Chem Mater* 26(1):277–286.
- Schumann M, Buckmann T, Gruhler N, Wegener M, Pernice W (2014) Hybrid 2D-3D optical devices for integrated optics by direct laser writing. *Light Sci Appl* 3:e175.
- Fan Z, et al. (2009) Three-dimensional nanopillar-array photovoltaics on low-cost and flexible substrates. *Nat Mater* 8(8):648–653.
- Bishop D, Pardo F, Bolle C, Giles R, Aksyuk V (2012) Silicon micro-machines for fun and profit. *J Low Temp Phys* 169(5–6):386–399.
- Wood RJ (2014) The challenge of manufacturing between macro and micro. *Am Sci* 102(2):124–131.
- Piyawattanametha W, Patterson PR, Hah D, Toshiyoshi H, Wu MC (2005) Surface- and bulk-micromachined two-dimensional scanner driven by angular vertical comb actuators. *J Microelectromech Syst* 14(6):1329–1338.
- Zheng X, et al. (2014) Ultralight, ultrastiff mechanical metamaterials. *Science* 344(6190):1373–1377.
- Schaedler TA, et al. (2011) Ultralight metallic microlattices. *Science* 334(6058):962–965.
- Soukoulis CM, Wegener M (2011) Past achievements and future challenges in the development of three-dimensional photonic metamaterials. *Nat Photonics* 5(9):523–530.
- Valentine J, et al. (2008) Three-dimensional optical metamaterial with a negative refractive index. *Nature* 455(7211):376–379.
- Cho JH, et al. (2011) Nanoscale origami for 3D optics. *Small* 7(14):1943–1948.
- Ahn BY, et al. (2009) Omnidirectional printing of flexible, stretchable, and spanning silver microelectrodes. *Science* 323(5921):1590–1593.
- Huang W, et al. (2012) On-chip inductors with self-rolled-up SiN_x nanomembrane tubes: A novel design platform for extreme miniaturization. *Nano Lett* 12(12):6283–6288.
- Grimm D, et al. (2013) Rolled-up nanomembranes as compact 3D architectures for field effect transistors and fluidic sensing applications. *Nano Lett* 13(1):213–218.
- Klein Y, Efrati E, Sharon E (2007) Shaping of elastic sheets by prescription of non-Euclidean metrics. *Science* 315(5815):1116–1120.
- Kim J, Hanna JA, Byun M, Santangelo CD, Hayward RC (2012) Designing responsive buckled surfaces by halftone gel lithography. *Science* 335(6073):1201–1205.
- Hawkes E, et al. (2010) Programmable matter by folding. *Proc Natl Acad Sci USA* 107(28):12441–12445.
- Ware TH, McConney ME, Wie JJ, Tondiglia VP, White TJ (2015) Actuating liquid. Voxelated liquid crystal elastomers. *Science* 347(6225):982–984.
- Leong TG, Zafarshar AM, Gracias DH (2010) Three-dimensional fabrication at small size scales. *Small* 6(7):792–806.
- Prinz VY, et al. (2001) A new technique for fabricating three-dimensional micro- and nanostructures of various shapes. *Nanotechnology* 12(4):399–402.
- Schmidt OG, Eberl K (2001) Nanotechnology. Thin solid films roll up into nanotubes. *Nature* 410(6825):168.
- Zhang X, et al. (2011) Optically- and thermally-responsive programmable materials based on carbon nanotube-hydrogel polymer composites. *Nano Lett* 11(8):3239–3244.
- Py C, et al. (2007) Capillary origami: Spontaneous wrapping of a droplet with an elastic sheet. *Phys Rev Lett* 98(15):156103.
- Sun Y, Choi WM, Jiang H, Huang YY, Rogers JA (2006) Controlled buckling of semiconductor nanoribbons for stretchable electronics. *Nat Nanotechnol* 1(3):201–207.
- Xu S, et al. (2015) Materials science. Assembly of micro/nanomaterials into complex, three-dimensional architectures by compressive buckling. *Science* 347(6218):154–159.
- Castle T, et al. (2014) Making the cut: Lattice kirigami rules. *Phys Rev Lett* 113(24):245502.
- Sussman DM, et al. (2015) Algorithmic lattice kirigami: A route to pluripotent materials. *Proc Natl Acad Sci USA* 112(24):7449–7453.
- Shyu TC, et al. (2015) A kirigami approach to engineering elasticity in nanocomposites through patterned defects. *Nat Mater* 14(8):785–789.
- Timoshenko S, Gere J (1961) *Theory of Elastic Stability* (McGraw-Hill, New York).
- Cho Y, et al. (2014) Engineering the shape and structure of materials by fractal cut. *Proc Natl Acad Sci USA* 111(49):17390–17395.
- Gottheim S, Zhang H, Govorov AO, Halas NJ (2015) Fractal nanoparticle plasmonics: The Cayley tree. *ACS Nano* 9(3):3284–3292.
- LaFratta CN, Fourkas JT, Baldacchini T, Farrer RA (2007) Multiphoton fabrication. *Angew Chem Int Ed Engl* 46(33):6238–6258.
- Lewis JA (2006) Direct ink writing of 3D functional materials. *Adv Funct Mater* 16(17):2193–2204.
- Tumbleston JR, et al. (2015) Additive manufacturing. Continuous liquid interface production of 3D objects. *Science* 347(6228):1349–1352.

Supplementary Information for

A mechanically driven form of Kirigami as a route to 3D mesostructures in micro/nanomembranes

Yihui Zhang^{a,1}, Zheng Yan^{b,1}, Kewang Nan^c, Dongqing Xiao^d, Yuhao Liu^b, Haiwen Luan^e, Haoran Fu^{e,f}, Xizhu Wang^b, Qinglin Yang^b, Jiechen Wang^b, Wen Ren^g, Hongzhi Si^b, Fei Liu^a, Lihen Yang^b, Hejun Li^g, Juntong Wang^c, Xuelin Guo^b, Hongying Luo^{e,h}, Liang Wang^{e,i}, Yonggang Huang^{e,2}, John A. Rogers^{b,d,j,2}

^aCenter for Mechanics and Materials, AML, Department of Engineering Mechanics, Tsinghua University, Beijing 100084, P.R. China.

^bDepartment of Materials Science and Engineering and Frederick Seitz Materials Research Laboratory, University of Illinois at Urbana-Champaign, Urbana, IL 61801, USA.

^cDepartment of Mechanical Science and Engineering, University of Illinois at Urbana-Champaign, Urbana, IL 61801, USA.

^dDepartment of Chemistry, University of Illinois at Urbana-Champaign, Urbana, IL 61801, USA.

^eDepartments of Civil and Environmental Engineering and Mechanical Engineering, Center for Engineering and Health, and Skin Disease Research Center, Northwestern University, Evanston, IL 60208, USA.

^fDepartment of Civil Engineering and Architecture, Zhejiang University, Hangzhou 310058, P.R. China.

^gDepartment of Chemical & Biomolecular Engineering, University of Illinois at Urbana-Champaign, Urbana, IL 61801, USA.

^hSchool of Aerospace Engineering and Applied Mechanics, Tongji University, Shanghai 200092, P.R. China.

ⁱInstitute of Chemical Machinery and Process Equipment, Zhejiang University, Hangzhou 310027, P.R. China.

^jBeckman Institute for Advanced Science and Technology, University of Illinois at Urbana-Champaign, Urbana, IL 61801, USA.

¹These authors contributed equally to this work.

²To whom correspondence may be addressed. E-mail: jrogers@illinois.edu or y-huang@northwestern.edu.

This PDF file includes:

Figures S1 to S23

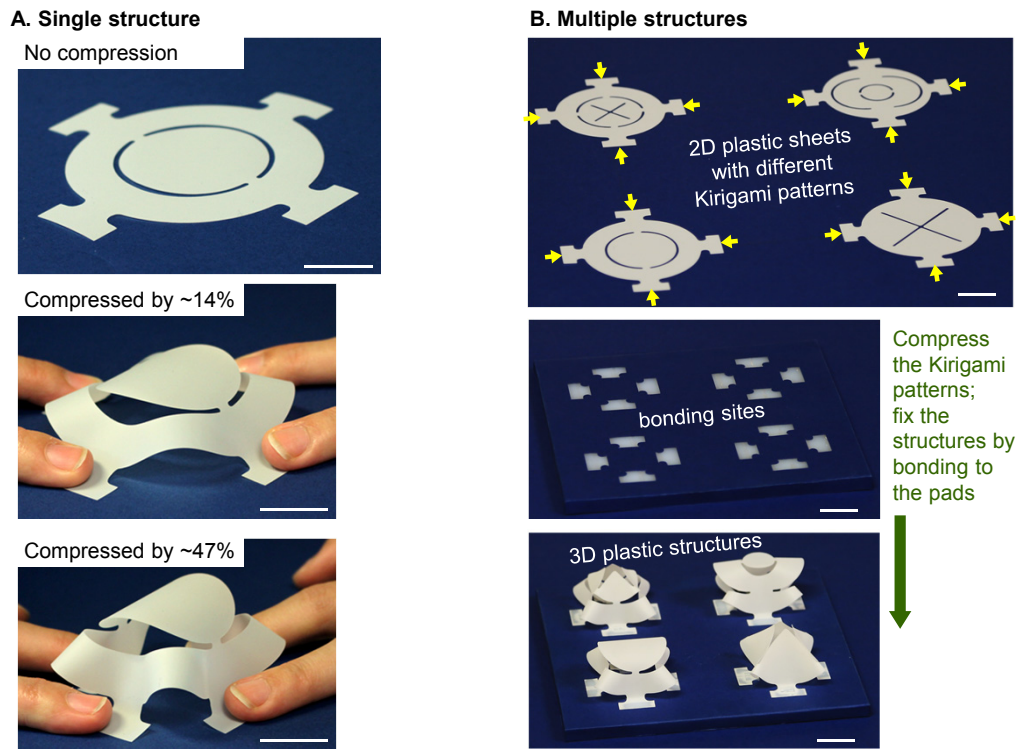


Figure S1. Illustration of the Kirigami process applied to macroscale sheets of plastic. (A) A thin ($\sim 80 \mu\text{m}$ thick) plastic film in a freestanding state and in states of bi-axially compressed (14% and 47%) induced by manual application of force. (B) Four 2D plastic precursors with the same overall shape but different Kirigami cuts, and the corresponding 3D structures under compression ($\sim 47\%$). All scale bars are 20 mm.

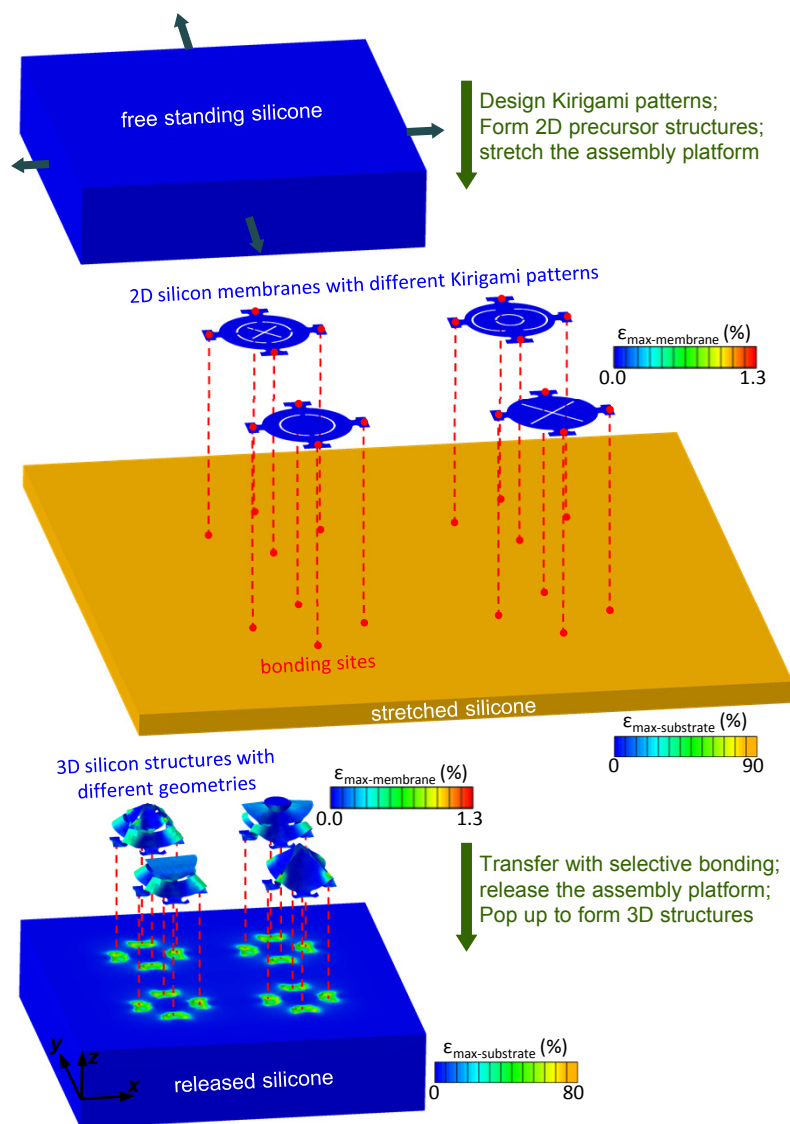
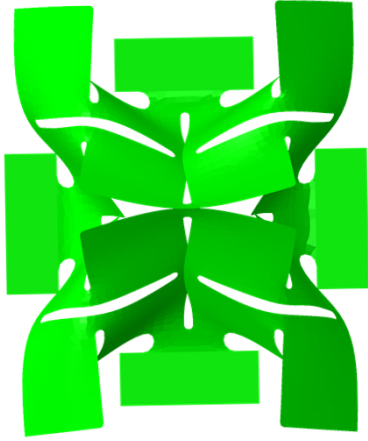
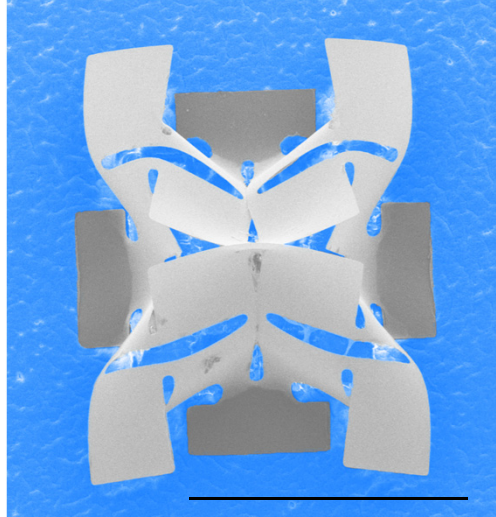


Figure S2. Finite-element analysis (FEA) results that illustrate the formation of 3D structures from 2D silicon nanomebranes (Si NMs) bonded at selected regions (red dots) to a biaxially stretched silicone elastomer. Compressive forces induced by relaxing the strain in the elastomer lead to coordinated out-of-plane deformations and translational motions in the Si NMs, yielding 3D structures with geometries that depend highly on the geometries of the 2D precursors and the Kirigami cuts in them.

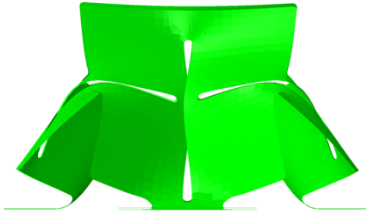
Top view (FEA)



Top view (SEM)



Front view (FEA)



Side view (FEA)

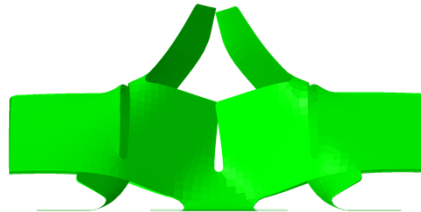
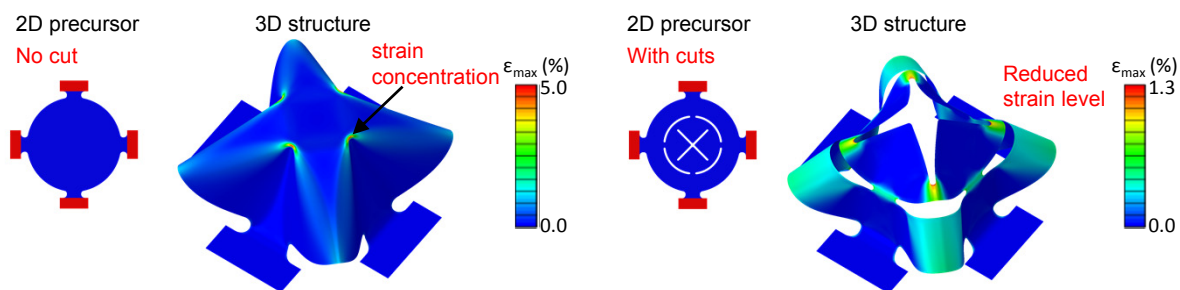


Figure S3. Images of the complex 3D membrane mesostructure in Fig. 1C, with three viewing angles that differ from the one in Fig. 1C. The scale bar is 200 μm .

A. 3D structures formed from two 2D circular membranes (one without and another with cuts)



B. 3D structures formed from two 2D square membranes (one without and another with cuts)

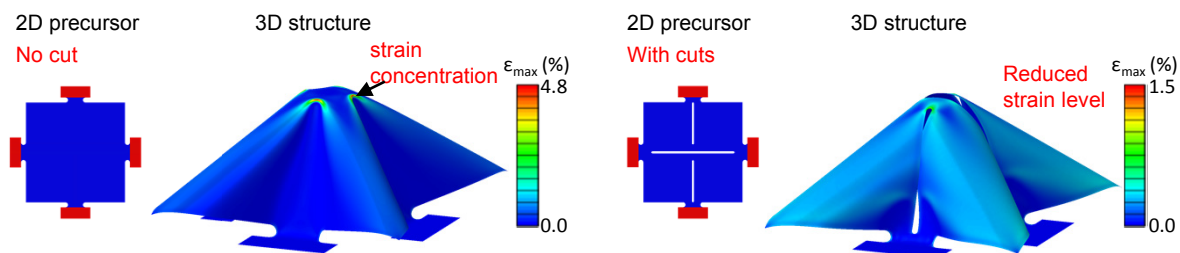
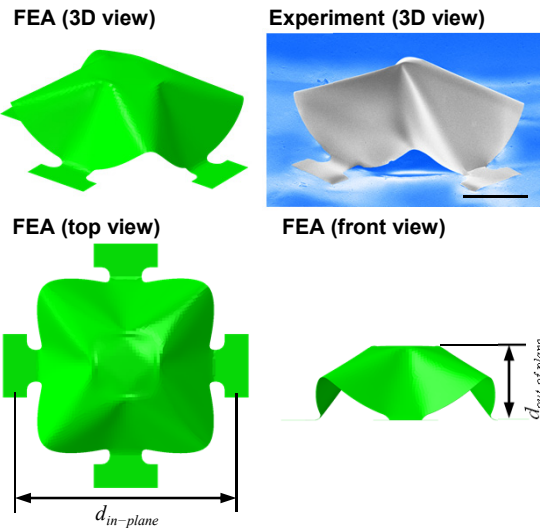


Figure S4. Illustration of the reductions in strains that follow from the use of Kirigami. (A) Comparison of strain distributions in the silicon layers of 3D structures formed with two different 2D circular membranes (left: without any cuts; right: with cuts). (B) Comparison of strain distributions in the silicon layers of 3D structures formed with two different 2D square membranes (left: without any cuts; right: with cuts). All of these structures incorporate bilayers of silicon/polymer (each ~ 300 nm in thickness). The prestrain used in all cases is 80%. The color represents the magnitude of the strain.

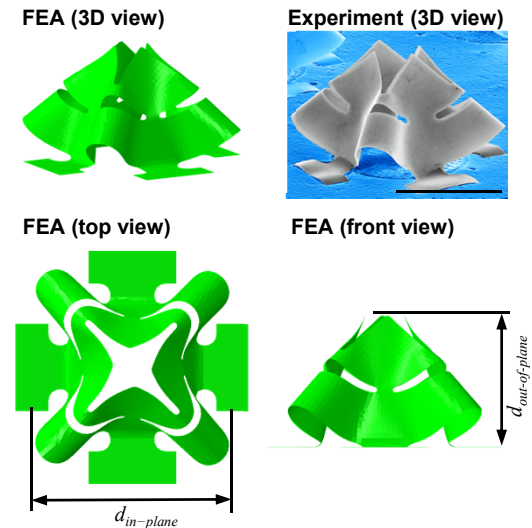
A. 3D structure formed from a 2D circular membrane without any cuts

$\epsilon_{pre}=35\%$, aspect ratio $d_{out-of-plane} / d_{in-plane} \approx 0.30$



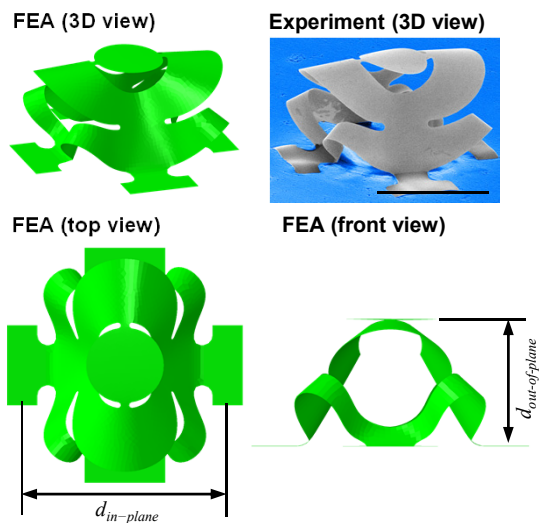
B. 3D structure formed from a 2D circular membrane with both radial and circumferential cuts

$\epsilon_{pre}=90\%$, aspect ratio $d_{out-of-plane} / d_{in-plane} \approx 0.68$



C. 3D structure formed from a 2D circular membrane with circumferential cuts

$\epsilon_{pre}=64\%$, aspect ratio $d_{out-of-plane} / d_{in-plane} \approx 0.53$



D. 3D structure formed from a 2D circular membrane with serpentine cuts

$\epsilon_{pre}=64\%$, aspect ratio $d_{out-of-plane} / d_{in-plane} \approx 0.62$

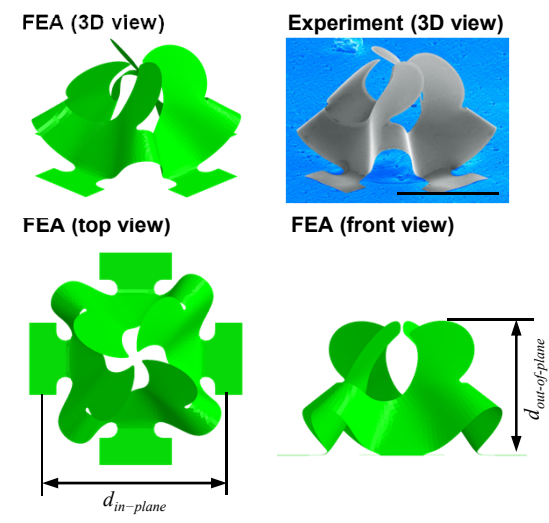


Figure S5. Effect of Kirigami design on the shapes of 3D structures. (A) Images with different viewing angles of a 3D structure formed from a 2D circular membrane without any Kirigami cuts and with a prestrain of 35%. (B) Images with different viewing angles of a 3D structure formed from a 2D circular membrane with both radial and circumferential cuts and with a prestrain of 90%. (C) Images with different viewing angles of a 3D structure formed from a 2D circular membrane with circumferential cuts and a prestrain of 64%. (D) Images with different viewing angles of a 3D structure formed from a 2D circular membrane with serpentine cuts and a prestrain of 64%. The design without any cuts yields a mesostructure with a basic, modest type of 3D configuration, as evidenced by the small aspect ratio ($\alpha = d_{out-of-plane} / d_{in-plane}$, where $d_{out-of-plane}$ and $d_{in-plane}$ denote the maximum out-of-plane dimension and in-plane extent, respectively; $\alpha = 0.3$ for the case shown here). This ratio is ~ 2.3 times smaller than that of the 3D structure formed with Kirigami cuts in (B). The scale bars in all SEM images are 200 μm .

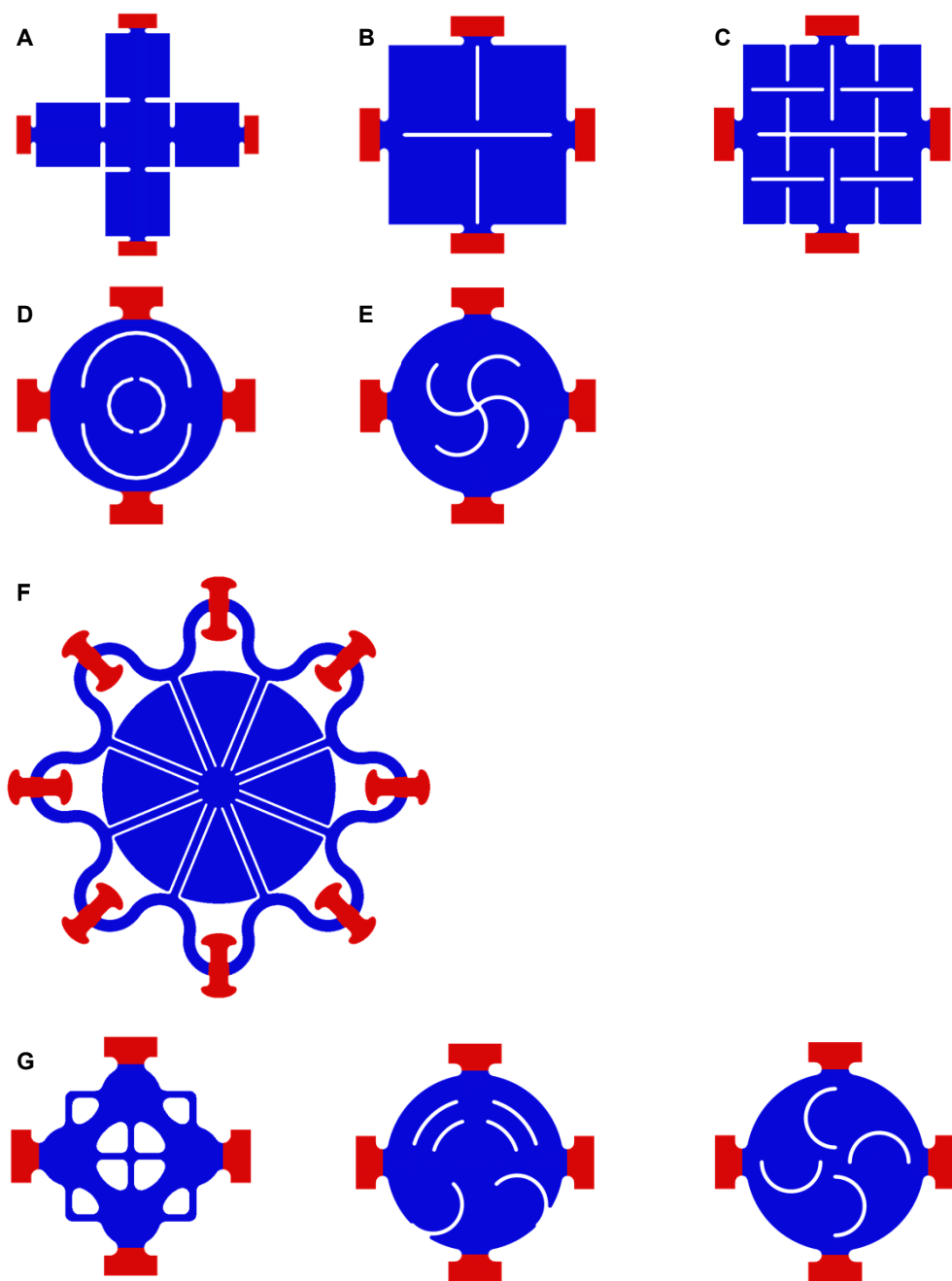


Figure S6. 2D precursor patterns for the 3D structures shown in Fig. 1 A-G, where the bonding regions are highlighted in red.

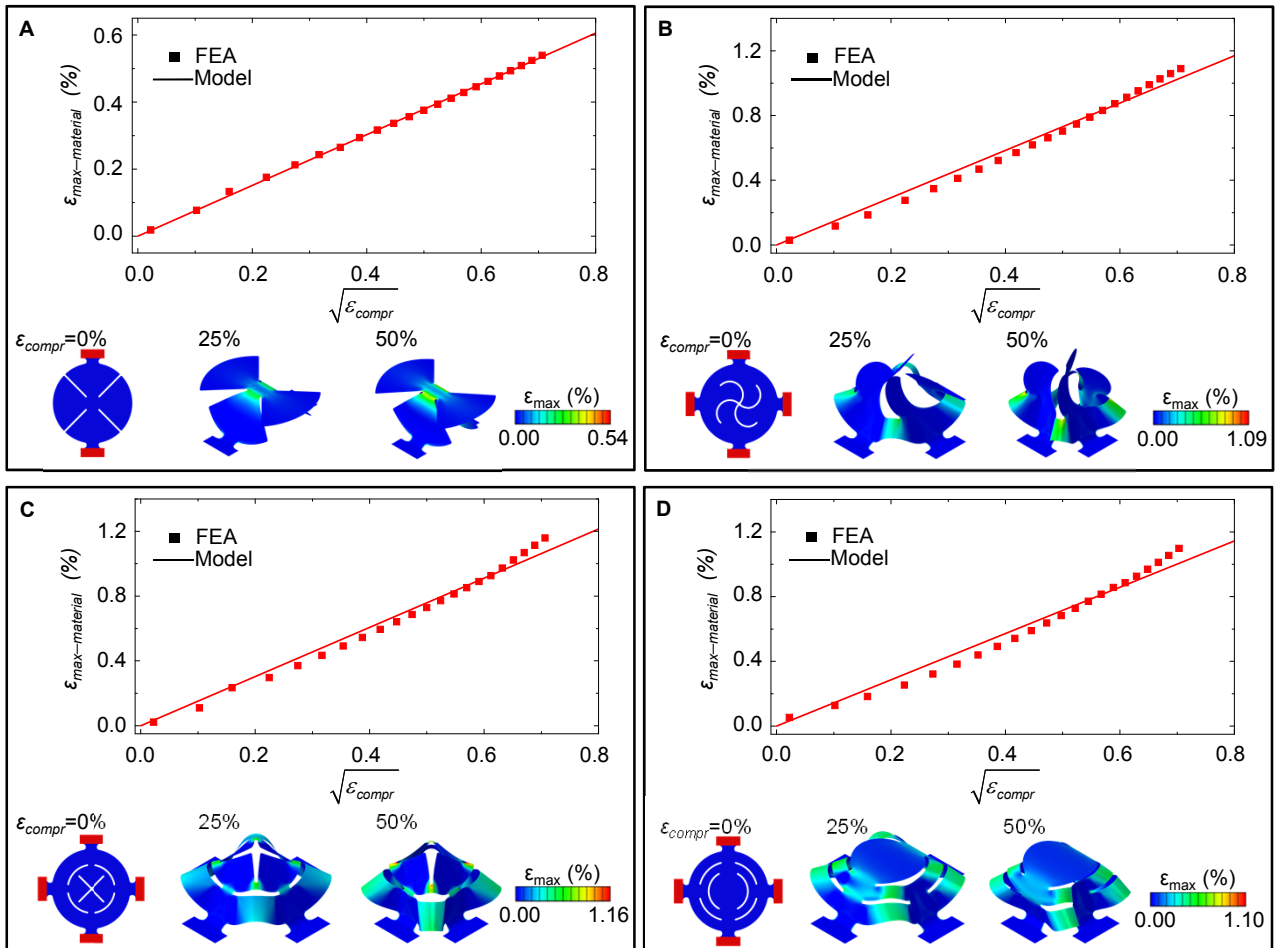


Figure S7. Maximum material strain as a function of the square root of the compressive strain, for various 3D structures formed using different Kirigami cuts: A) symmetric cuts along the radial direction (with $t/L = 0.0011$, $w_{cut}/L = 0.044$, and $l_{cut}/L = 0.77$); B) anti-symmetric cuts in a serpentine configuration (with $t/L = 0.0011$, $w_{cut}/L = 0.044$, and $l_{cut}/L = 1.03$); C) symmetric cuts partially along the radial direction and partially along the circumferential direction (with $t/L = 0.0011$, $w_{cut}/L = 0.044$, and $l_{cut}/L = 0.72$); D) symmetric cuts along the circumferential direction (with $t/L = 0.0011$, $w_{cut}/L = 0.044$, and $l_{cut}/L = 0.77$). The results show a proportional dependence of the maximum material strain on the square root of the compressive strain. For the Kirigami patterns in (C) and (D), the lengths (l_{cut}) correspond to the circumferential cuts located at the outer region of the membrane.

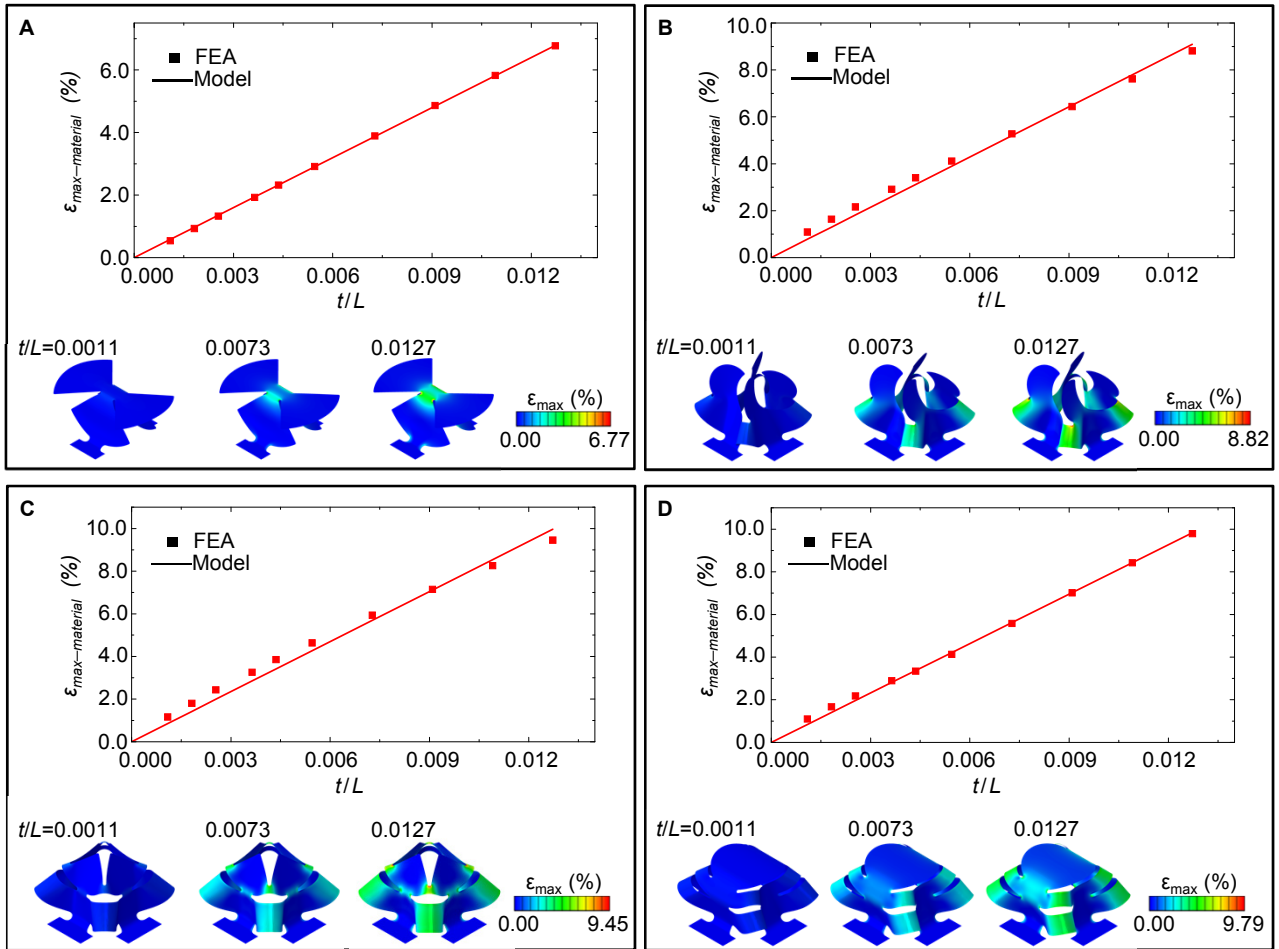


Figure S8. Maximum material strain as a function of dimensionless thickness, for various 3D structures formed using 100% prestrain (i.e., corresponding to 50% compressive strain) and different Kirigami patterns: A) symmetric cuts along the radial direction (with $w_{cut}/L = 0.044$ and $l_{cut}/L = 0.77$); B) anti-symmetric cuts in the serpentine configuration (with $w_{cut}/L = 0.044$ and $l_{cut}/L = 1.03$); C) symmetric cuts partially along the radial direction and partially along the circumferential direction (with $w_{cut}/L = 0.044$ and $l_{cut}/L = 0.72$); D) symmetric cuts along the circumferential direction (with $w_{cut}/L = 0.044$ and $l_{cut}/L = 0.77$). The results show a proportional dependence of the maximum material strain on the normalized thickness. For cases in (C) and (D), the lengths (l_{cut}) correspond to the circumferential cuts located at the outer region of the membrane.

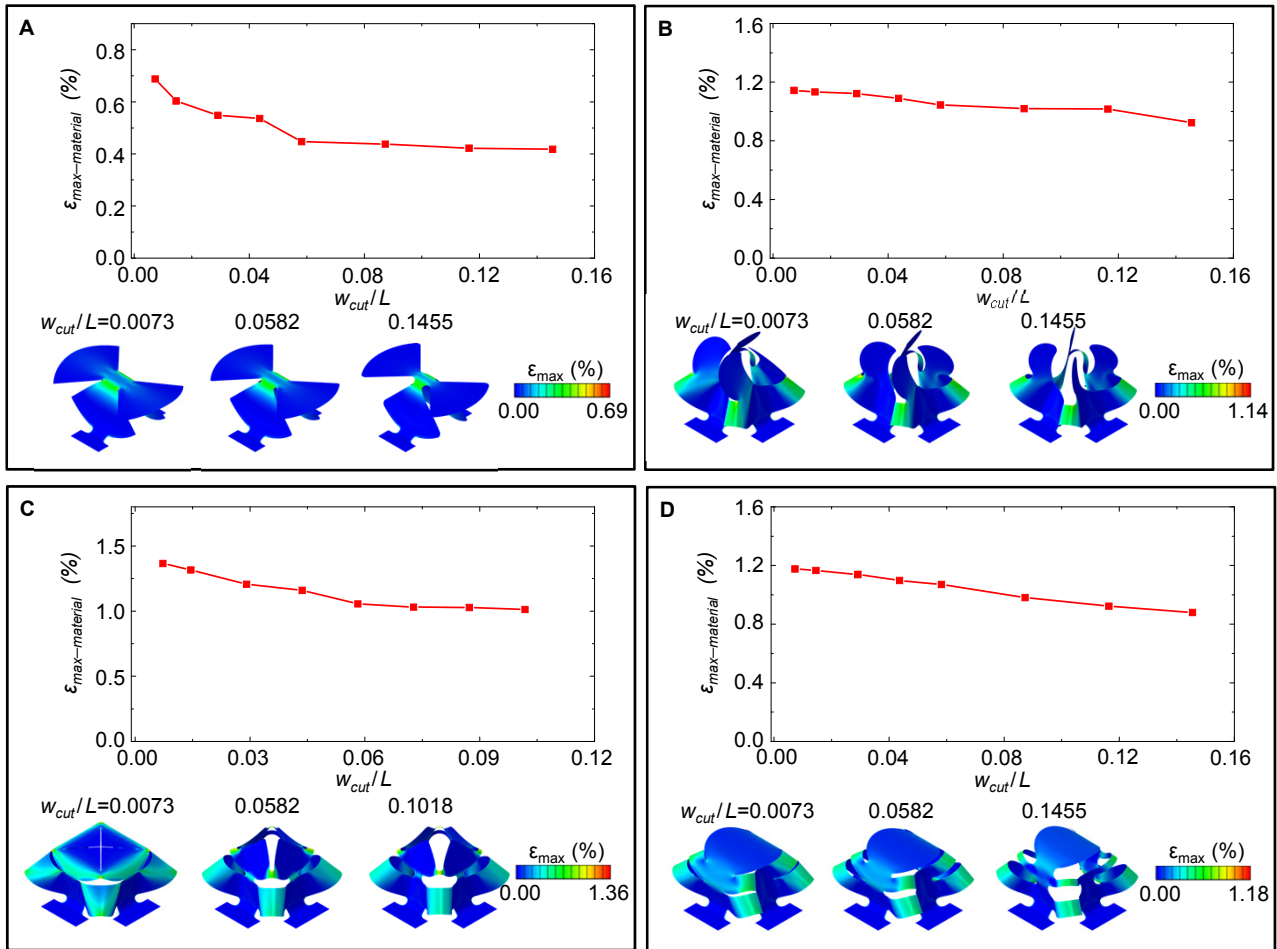


Figure S9. Maximum material strain as a function of dimensionless cut width, for various 3D structures formed using 100% prestrain (i.e., corresponding to 50% compressive strain) and different Kirigami patterns: A) symmetric cuts along the radial direction (with $t/L = 0.0011$ and $l_{\text{cut}}/L = 0.77$); B) anti-symmetric cuts in the serpentine configuration (with $t/L = 0.0011$ and $l_{\text{cut}}/L = 1.03$); C) symmetric cuts partially along the radial direction and partially along the circumferential direction (with $t/L = 0.0011$ and $l_{\text{cut}}/L = 0.72$); D) symmetric cuts along the circumferential direction (with $t/L = 0.0011$ and $l_{\text{cut}}/L = 0.77$). The results show that the material strain decreases with increasing cut width. For the cases in (C) and (D), the lengths (l_{cut}) correspond to the circumferential cuts located at the outer region of the membrane.

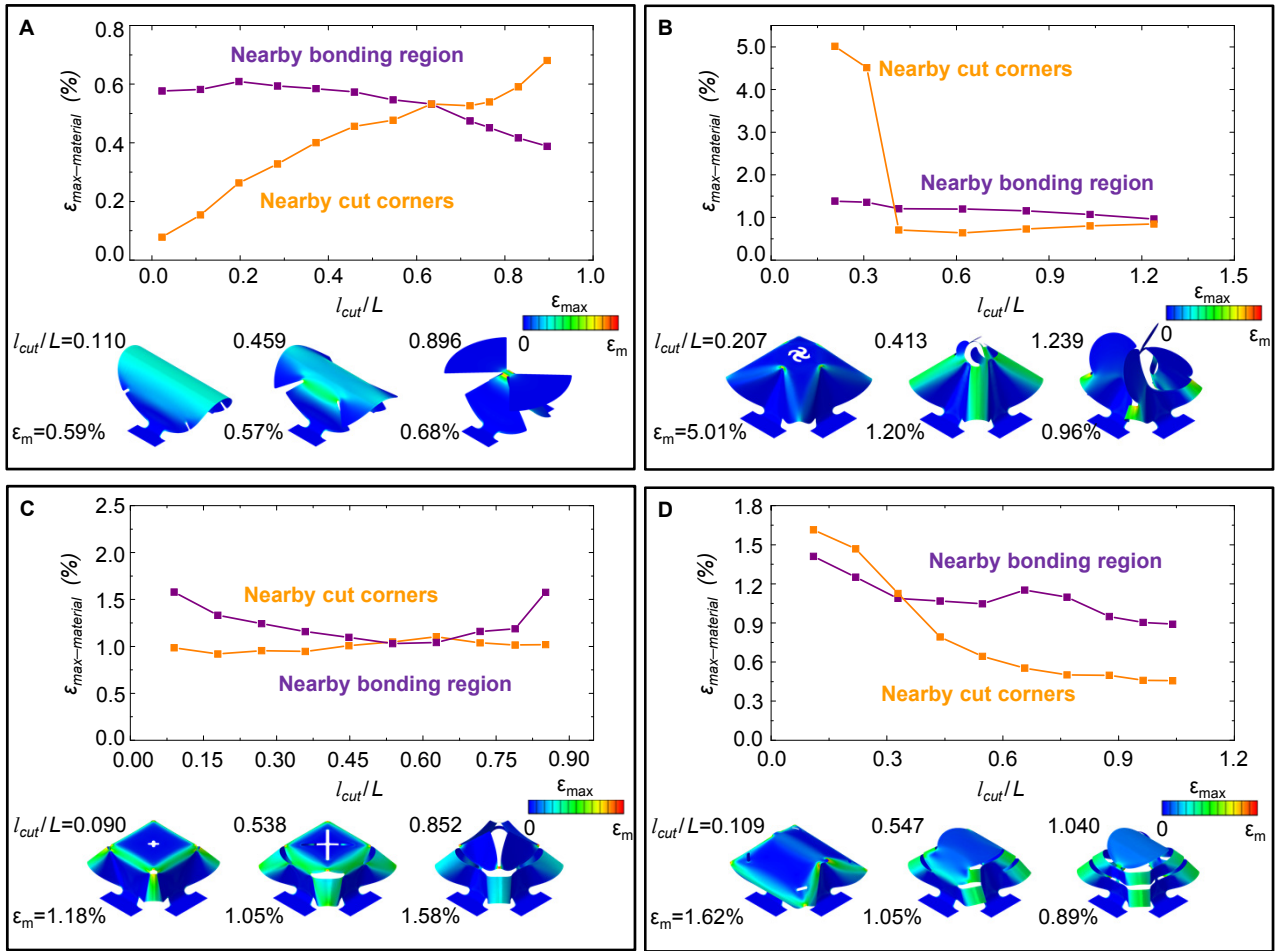


Figure S10. Maximum material strains near the corners of the Kirigami cuts and near the bonding region as a function of the dimensionless cut length, for various 3D structures formed using 100% prestrain (i.e., corresponding to 50% compressive strain) and different Kirigami patterns: A) symmetric cuts along the radial direction (with $t/L = 0.0011$ and $w_{cut}/L = 0.044$); B) anti-symmetric cuts in the serpentine configuration (with $t/L = 0.0011$ and $w_{cut}/L = 0.044$); C) symmetric cuts partially along the radial direction and partially along the circumferential direction (with $t/L = 0.0011$ and $w_{cut}/L = 0.044$); D) symmetric cuts along the circumferential direction (with $t/L = 0.0011$ and $w_{cut}/L = 0.044$). For the cases in (C) and (D), the lengths (l_{cut}) correspond to the circumferential cuts that are located at the outer region of the membrane. The lengths of the inner cuts scale with those of the outer cuts, with both reaching the corresponding limit (i.e., representing a throughout cut) simultaneously.

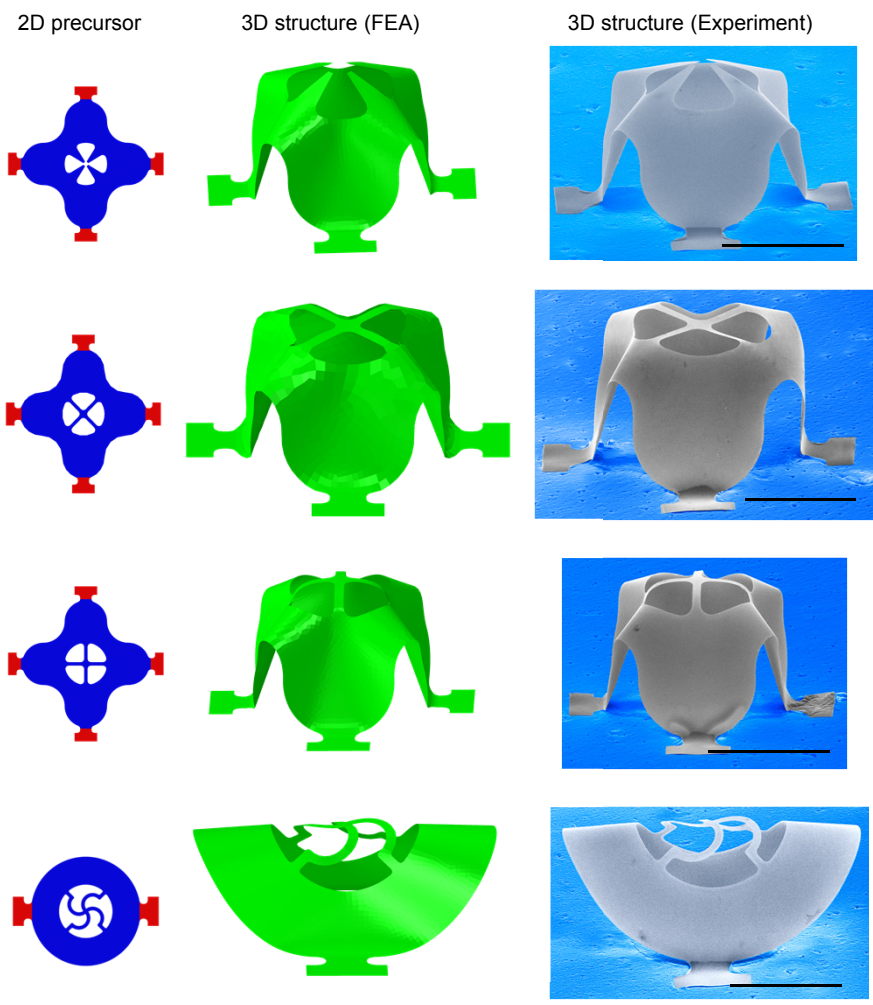
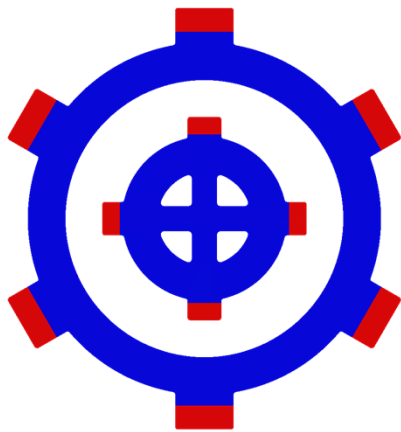


Figure S11. Four 3D structures (with hybrid configurations consisting of both membranes and ribbons) and their corresponding FEA results. The scale bars in all images are 200 μm .

A. 2D precursor



B. 3D configurations

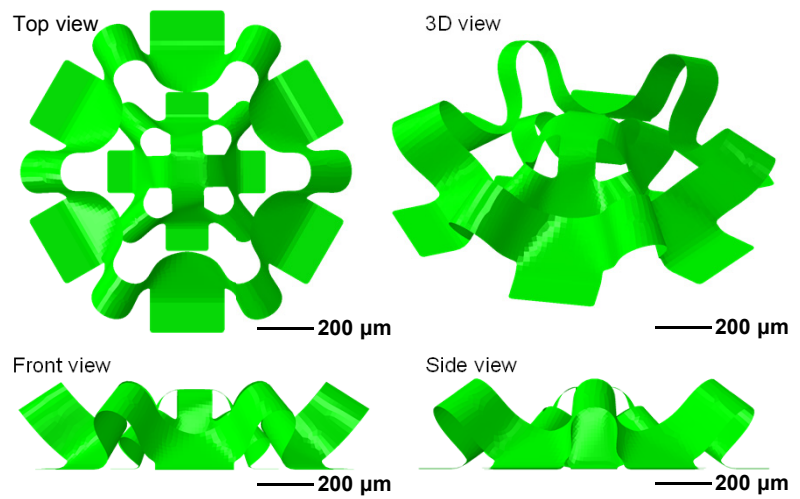


Figure S12. (A) 2D precursor for complex architecture with a geometry that resembles a 'crown', as shown in the top middle panel of Fig. 4B, where the bonding regions are highlighted in red. (B) Images of the 3D configurations with four different viewing angles.

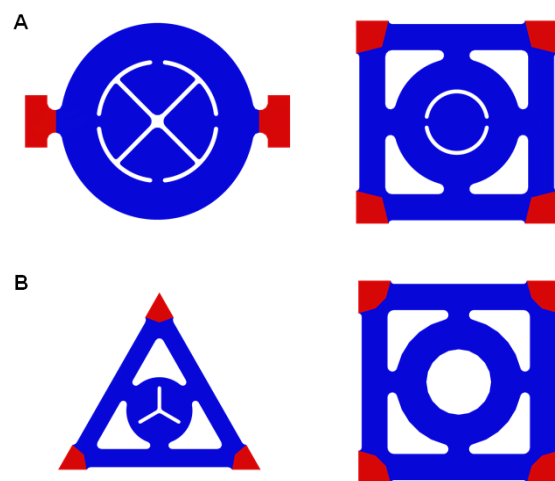
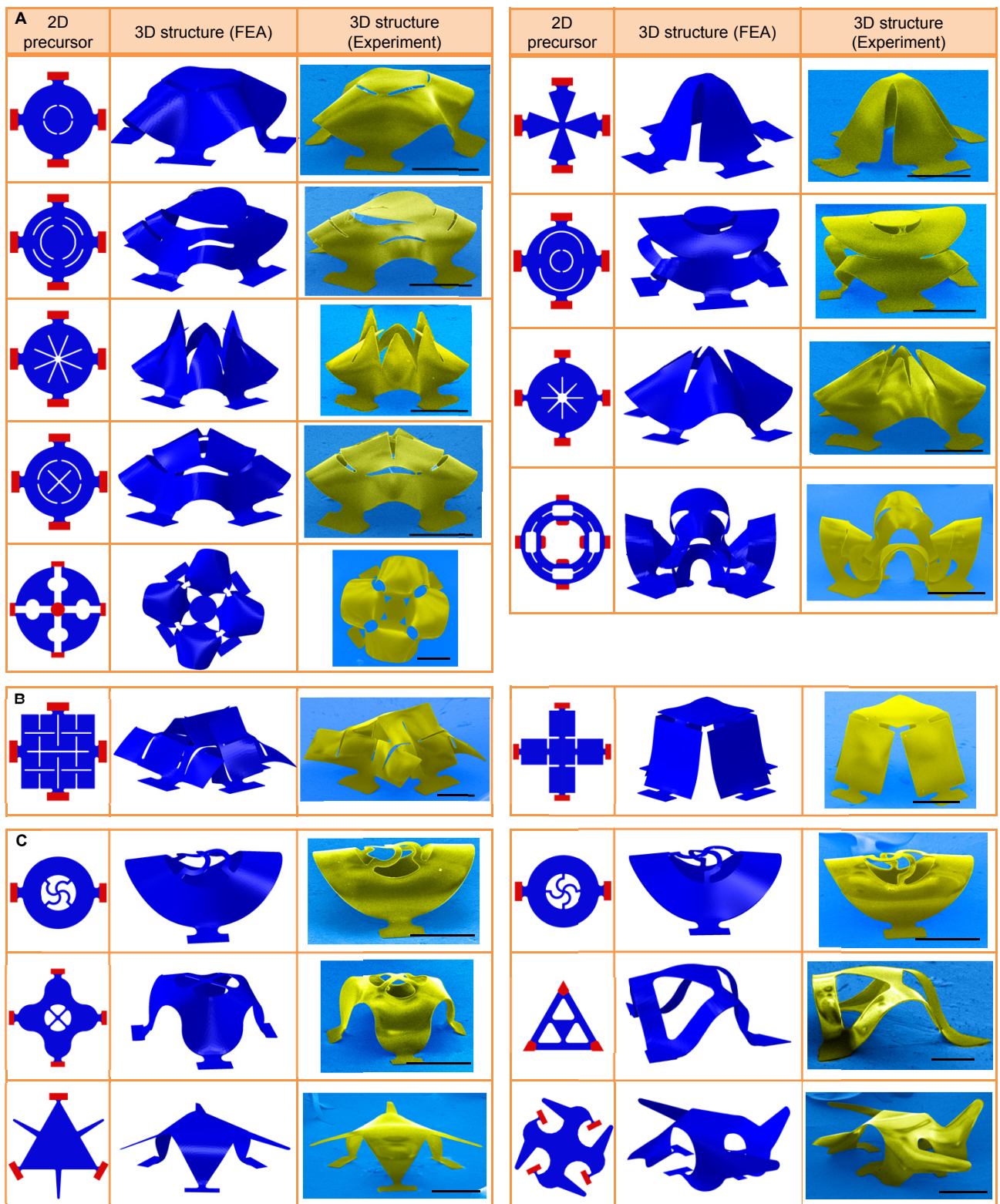


Figure S13. 2D precursors for the four 3D structures shown in Fig. 5A (A) and in Fig. 5B (B), where the bonding sites are highlighted in red.



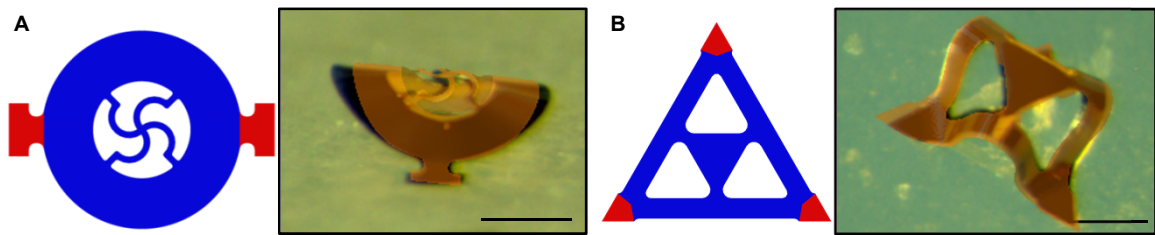


Figure S15. Comparison between experimental images and FEA predictions for two 3D structures (made from Au). The scale bars in all images are 200 μm .

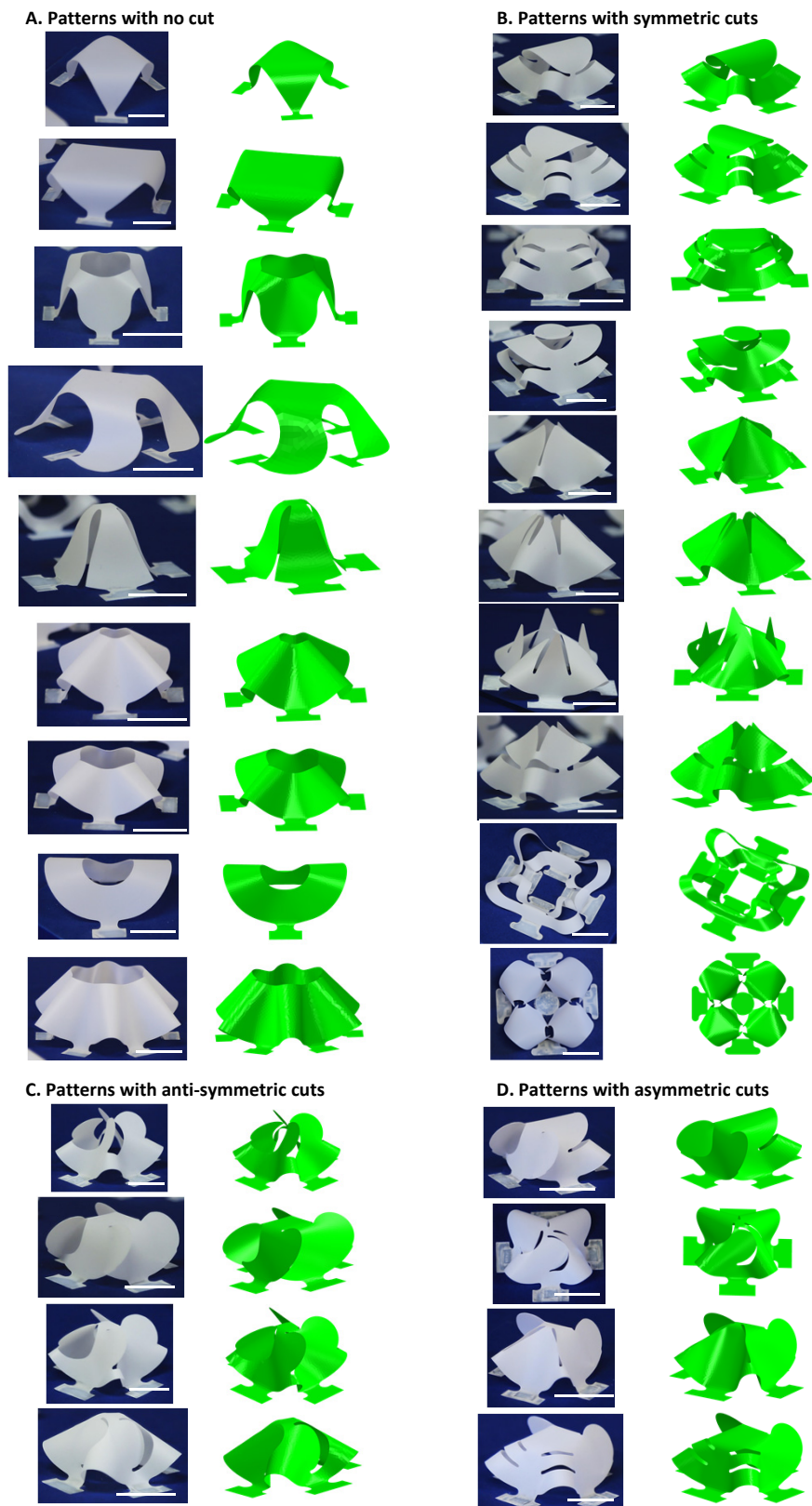


Figure S16. Comparison between experimental images and FEA predictions for various 3D structures made from plastic films at macroscale. The scale bars in all images are 20 mm.

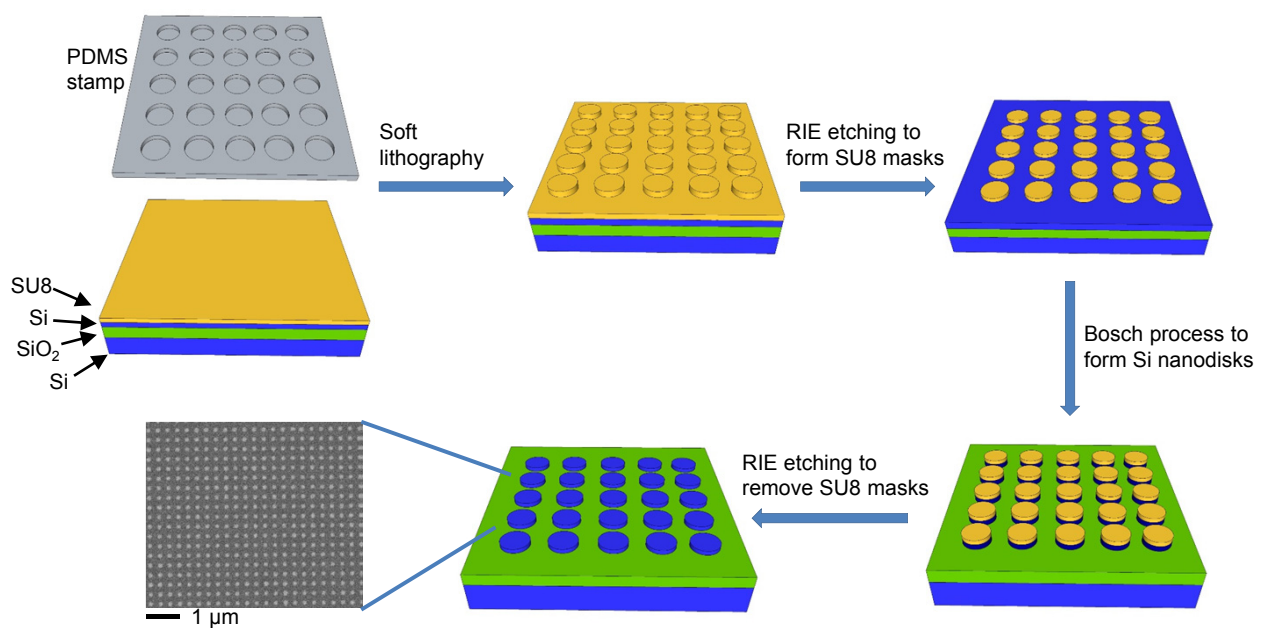


Figure S17. Process steps for making silicon nanodisks on a silicon-on-insulator wafer (200 nm thicknesses of silicon) by soft lithography. The diameters of the nanodisks are 200 nm.

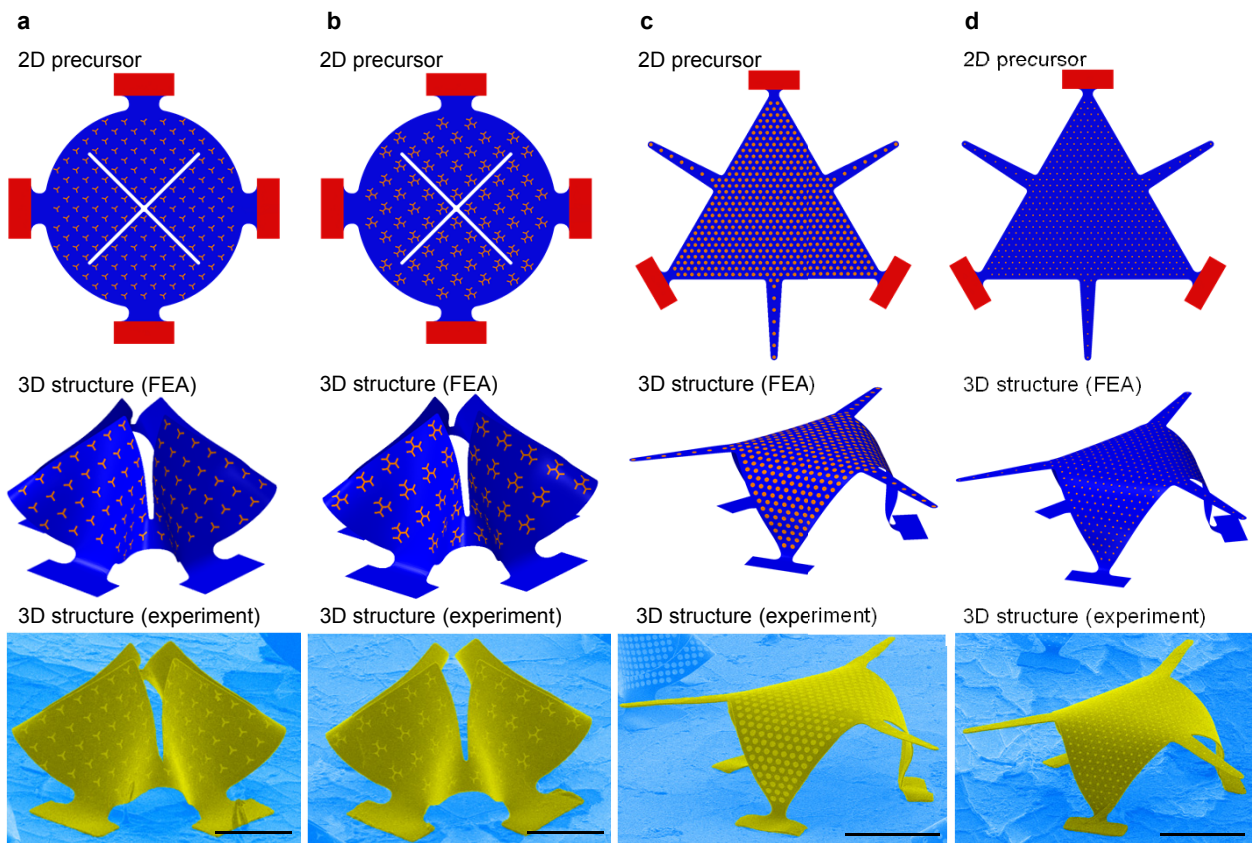


Figure S18. Comparison between experimental images and FEA predictions for four hybrid 3D structures of polymer (SU8) and patterned Au. The scale bars in both images are 200 μm .

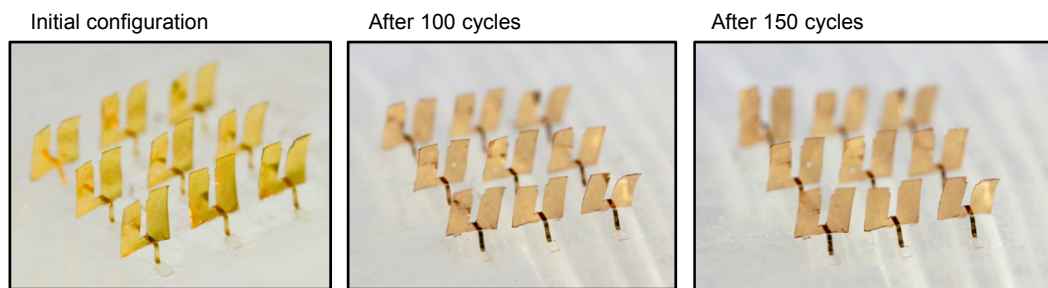


Figure S19. Cyclic testing of an optical transmission window with engineered thickness variations, under uniaxial strain with an amplitude of $\sim 65\%$ at a frequency of ~ 0.04 Hz. The three images correspond to the initial state, and the states after 100 and 150 cycles.

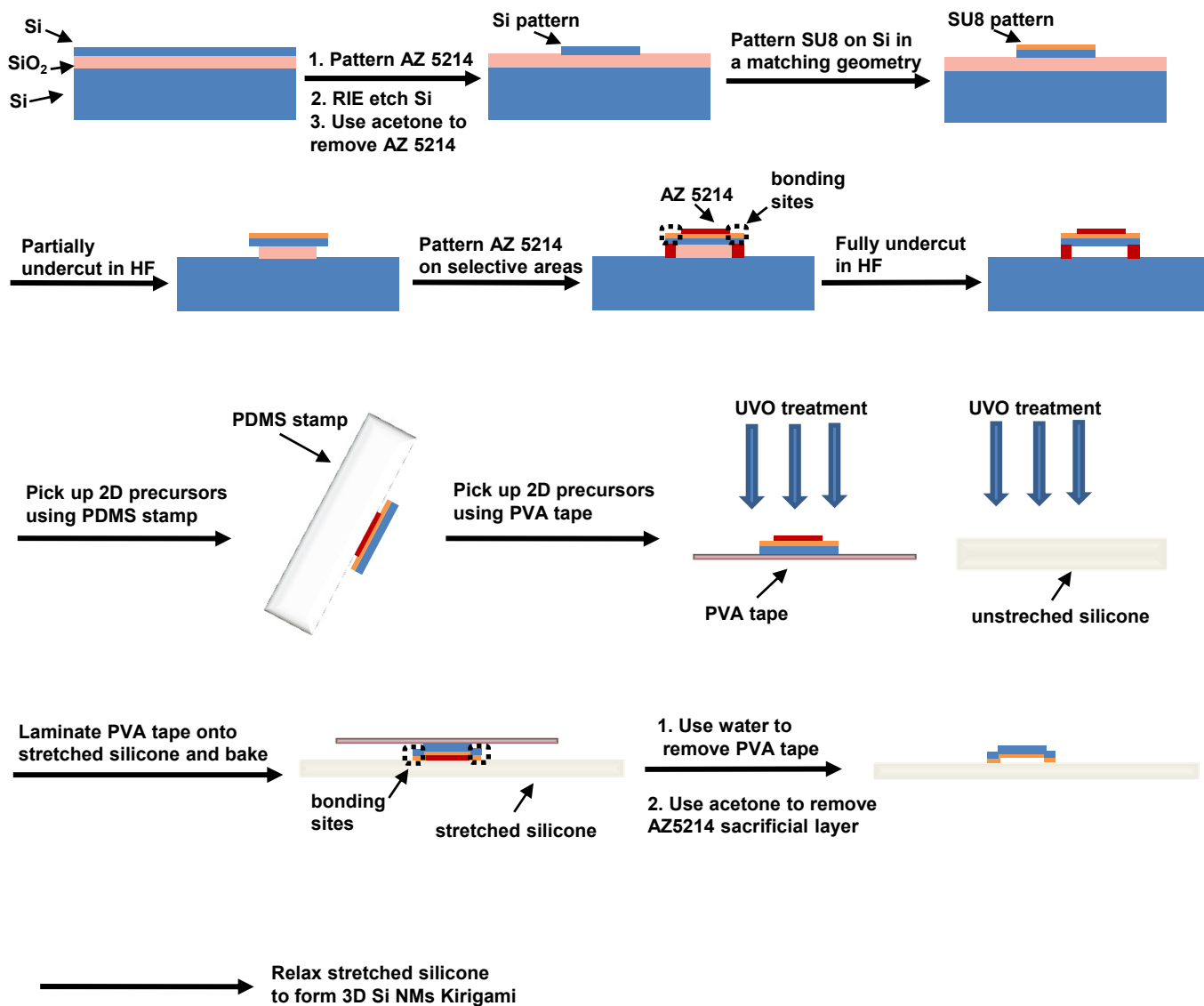


Figure S20. Schematic illustration of steps for fabricating 3D Kirigami structures of bilayers of Si NMs and layers of polymer (SU8).

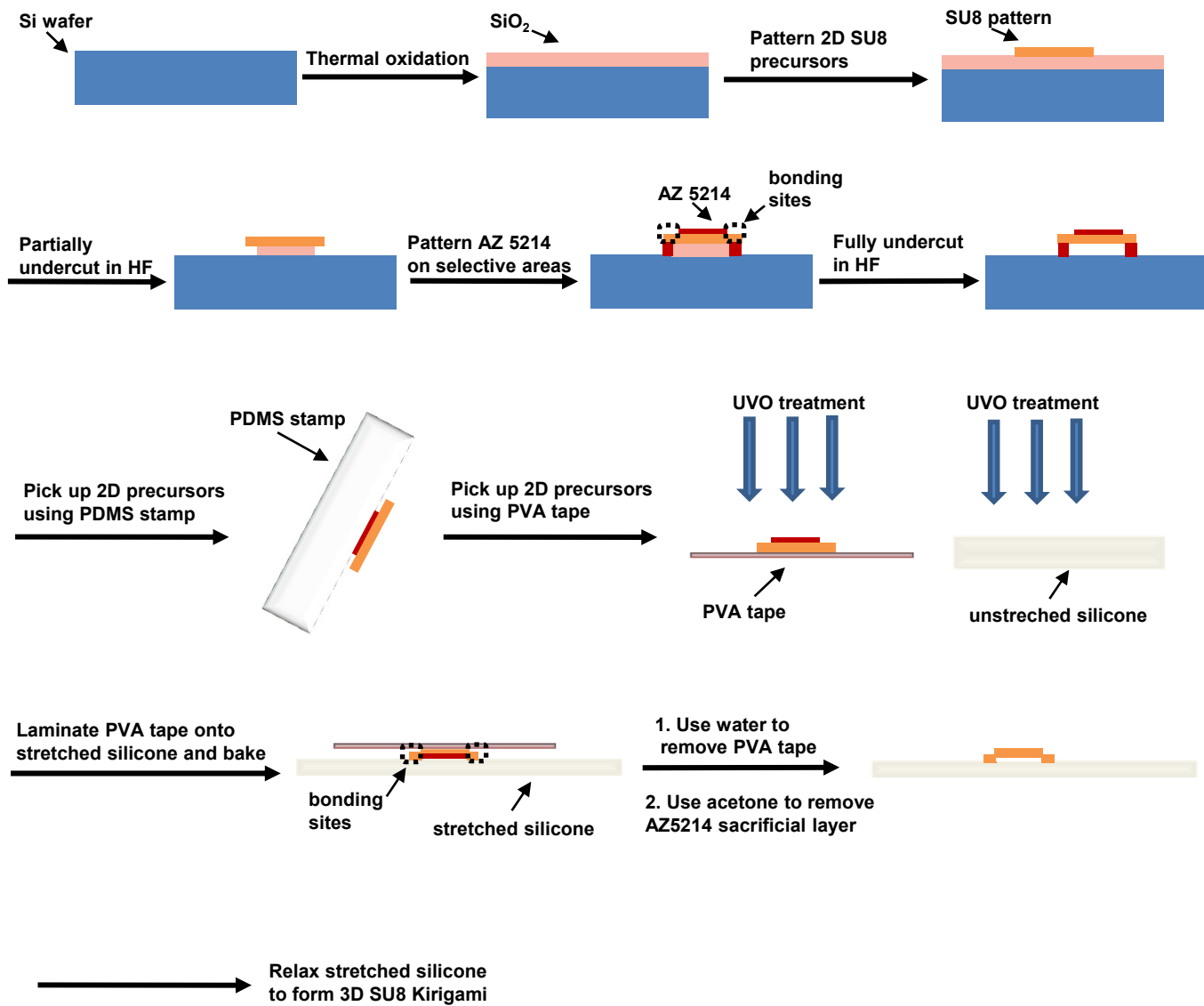


Figure S21. Schematic illustration of steps for fabricating 3D Kirigami structures of polymer (SU8).

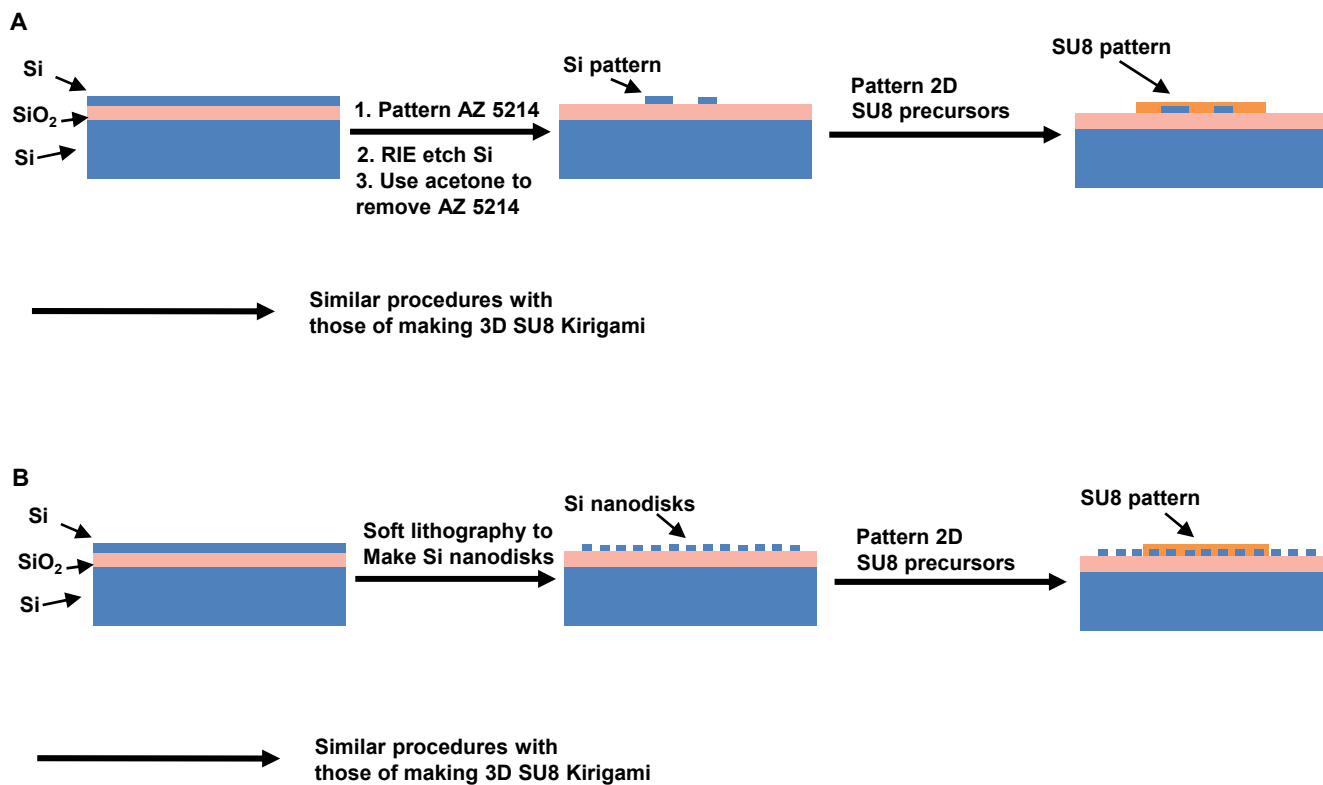


Figure S22. (A) Schematic illustration of steps for fabricating 3D hybrid Kirigami structures of Si NMs and polymer (SU8), as shown in Fig. 5C. (B) Schematic illustration of steps for making 3D hybrid Kirigami structures of Si nanodisks on layers of polymer (SU8) as shown in Fig. 5D.

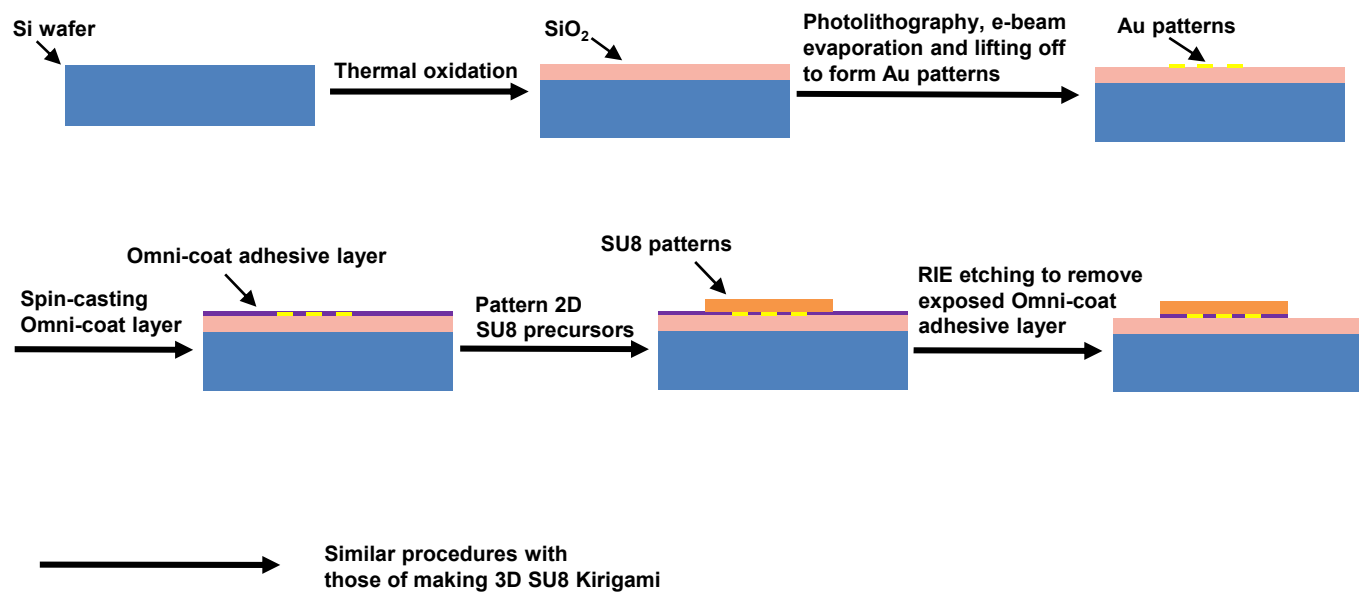


Figure S23. Schematic illustration of steps for fabricating 3D Kirigami structures of Au and polymer (SU8).